Commissioning of Ultra-Cold Neutron Asymmetry Spectrometer

Jennifer Ying Hsiao
Mentor: *Bradley Filippone*, Co-Mentor: *Brad Plaster*

Abstract

We can feasibly probe for physics beyond the Standard Model of particle physics with more accurate and precise results from neutron beta decay experiments. An ultracold neutron (UCN) beta decay experiment will begin this year at the Los Alamos Neutron Science Center (LANSCE). This experiment will perform a precision measurement of the neutron beta-asymmetry (or the A-correlation), which is the correlation between the neutron's spin and the momentum of the emitted decay electron. A precise measurement of the A-correlation, combined with a value for the neutron lifetime, can be used to test the unitarity of the Standard Model's quark-electroweak mixing matrix. Prior to commencement, the 1 Tesla field superconducting spectrometer constructed for the experiment by Caltech must be fully calibrated. A position and energy resolution study of the plastic scintillator and MWPC was accomplished using thin film conversion line sources, ^{113}Sn and ^{207}Bi, placed at the center of the spectrometer.

Introduction

The Importance of A

The Standard Model (SM) of the strong and electroweak interactions with its three generations of quarks and leptons has proven to be a triumph for particle physics. Indeed, the SM has enjoyed a great deal of phenomenological success, with one of its most notable achievements being the successful prediction of the mass range for the top quark, (the last undiscovered quark and the heaviest quark with a mass ~180 times that of the proton) prior to its discovery in high-energy proton-antiproton collisions at the Fermilab Tevatron in 1995.

Despite this success, the SM possesses a number of unsatisfying features – some examples include the unexplained origin of mass, the lack of unification with gravity, the cosmological phenomena of dark matter, and the abundance of matter over anti-matter in the universe (the so-called baryon asymmetry of the universe). As such, it is now widely believed that the SM is "incomplete" and, as a result, much effort is now focused on the search for new physics beyond the SM.

Searches for new physics beyond the SM can be performed either directly at high energies via the search for new, heavier particles produced in high-energy particle collisions or indirectly at lower energies via the comparison of precision measurements of fundamental quantities with SM predictions. One area in which the SM can be probed is neutron beta decay. Measurements of angular correlations in neutron beta decay can place constraints on the existence of right-handed currents, the presence of scalar and tensor terms in the weak interaction, and for evidence of time reversal violation, which is expected from the observed violation of charge-conjugation/parity invariance in kaon decay.

One possible strategy in searching for new physics beyond the SM is to measure known quantities with ever increasing accuracy and precision with the hope of detecting a difference between the SM predictions and the measurements. Another strategy is to probe for effects that are not included in the SM, but are predicted by the Grand Unified field Theories. Angular correlation measurements in neutron beta decay provide a means to pursue both strategies. By accurately and precisely measuring the coefficients of the allowed angular correlations (electron-neutrino, spin-electron, and spin-neutrino) we can search for the presence of right-handed currents and scalar and tensor terms in the weak interaction. All of these correlations are non-zero with a value precisely defined in the SM. By searching for a time-reversal-violating correlation coefficient (which is expected to be zero in the SM), we can test for the existence of time reversal violation. Thus, the need for experiments with ever increasing accuracy and precision in neutron beta decay is clear.

In the past few years, the development of more intense sources of cold and ultracold neutrons (UCN), and the invention of new trapping and detection techniques have enabled measurement of the characteristics of neutron beta decay at a new level of precision. An UCN beta decay experiment will begin this year at the Los Alamos Neutron Science Center (LANSCE). This experiment will perform a precision measurement of the neutron beta-asymmetry (or the A-correlation), which is the correlation between the neutron's spin and the momentum of the emitted decay electron. This will be the first correlation experiment performed with UCN. A precise measurement of the A-correlation, combined with a value for the neutron lifetime, can be used to test the unitarity of the Standard Model's quark-mass-eigenstate mixing matrix. Prior to commencement, studies must be made of the UCN source in order to optimize the number of UCNs we are producing. In addition, the superconducting spectrometer constructed for the experiment must be fully calibrated to determine its energy response function.

UCNA Experiment/Spectrometer Description

In the experiment, diamond-coated UCN guide tubes will transport UCN from the SD2 source to the beta asymmetry spectrometer. The UCN will be ~100% polarized by passage through a 7 T superconducting solenoid (pre-polarizing magnet, PPM). After passing through an Adiabatic Fast Passage (AFP) resonator that will allow rapid spin flipping of the UCN, the UCN will be fed to the center of the beta asymmetry spectrometer, as shown in Fig. 1.

The beta asymmetry spectrometer, or SuperConducting Spectrometer (SCS), consists of a 3-m long, 10-cm diameter UCN open-ended trap that defines a decay volume for the UCN, as shown in Fig. 1. A highly-uniform ($< 10^{-3}$ variation) strong (1.0 T) magnetic field is generated along the axis of the UCN trap by a superconducting solenoid. At the ends of the bottle, the magnetic field is expanded (from 1 T to 0.6 T) in the region before the detector to reduce backscattering. The strong magnetic field in the solenoid is used to determine the neutron spin direction and is used to guide the betas from neutron decay in the bottle to the detectors. Two detector systems will be used to measure the energy of the betas: scintillator and Si-strip detectors. The Si-strip detectors will provide an important systematic check on the performance and calibration of the spectrometer. In the principal detector configuration the betas are detected in a Multi-Wire Proportional Chamber (MWPC) - scintillator system at the ends of the spectrometer in the expanded field region. This detector system allows both position information from the multi-wire

proportional counters (MWPC), total energy information (from the scintillator), and some information on the pitch angle of the electron (from the dE/dx measurement in the MWPC). To distinguish between the two ends of the spectrometer, and between the two detector packages, we label one end the east and the other the west.

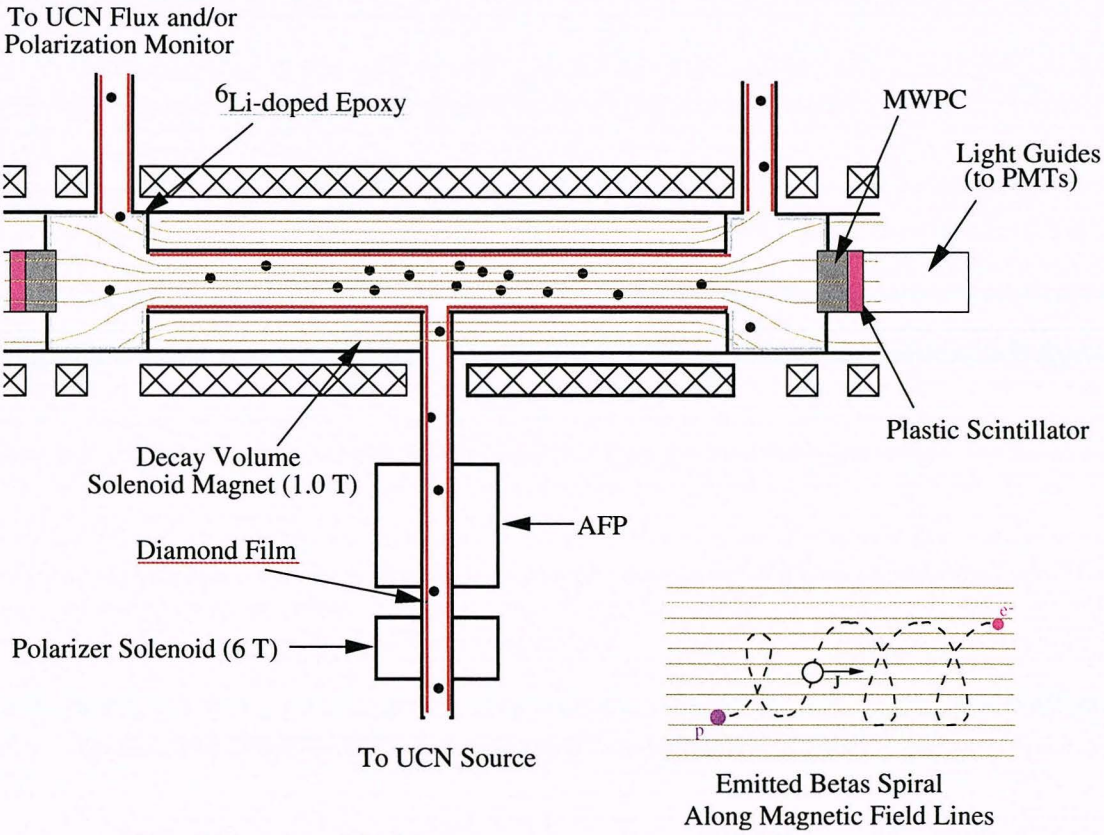

Figure 1 Top view of the beta asymmetry spectrometer (SCS)

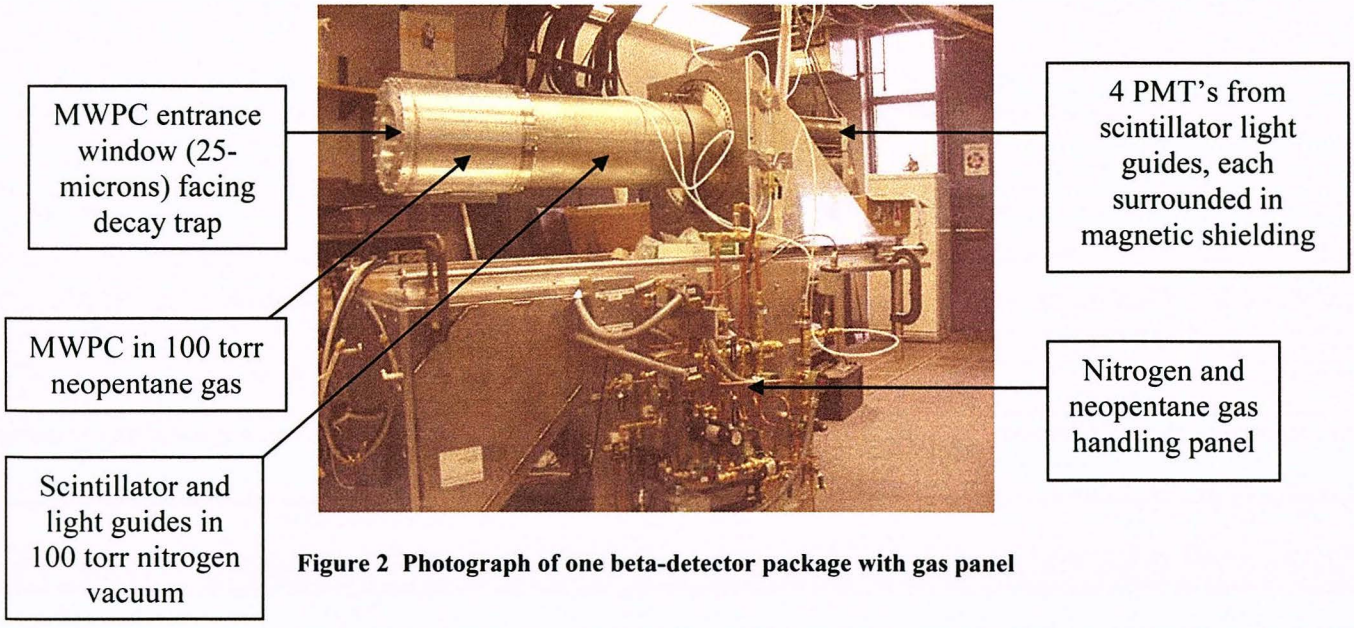

Figure 2 Photograph of one beta-detector package with gas panel

SCS /Beta-detector Description

The SCS volume, separated from the detector package by the MWPC front window, is kept in vacuum ($<10^{-5}$ Torr). The SCS magnet is cooled to superconducting temperatures with a liquid Helium (LHe) recirculation system. This elaborate refrigeration system takes the boil off helium gas from the SCS, stores it in medium pressure storage tanks until it can be compressed back into liquid helium by the helium refrigerator, and redistributes the LHe back into the SCS. This LHe system also recirculates LHe into the PPM and AFP magnets, as well as into the neutron source. At present, each time the SCS must be refilled (the LHe level sensor for the SCS must not reach below 70% at full field strength, 1 Telsa), the main solenoid must be ramped down slowly to avoid a quenching of the magnet (instantaneous discharging of all the magnet's energy to its surroundings). Thus, to fill the SCS, we must also stop the data acquisition system (DAQ).

The main detector system is shown in figure 3. The wire chambers for the beta detector are an important component of the experiment because they define the counting volume, and in coincidence with the plastic scintillator they minimize the background. In addition, they provide position information, have a low sensitivity to gamma rays, and have low mass and average Z to minimize electron backscattering.

The multi-wire proportional chamber detectors consist of a gas volume approximately 2 cm thick with a 25μm thin entrance window and a 25μm thin exit foil. In the center there is a plane of anode wires with a 1 mm separation of 10 micron diameter gold plated tungsten spaced in order to minimize the wires as a source of backscattering. The cathode wires are spaced ~5 mm apart, and the signals are read out from the scintillator. While the anode wires together provide the energy deposition information of each event, the 2 cathode planes give the X-Y position of the event, with wires in the 2 cathode planes orthogonal to each other. Each cathode strip is connected to a preamplifier, discriminator, and a peak sensing anode-to-digital converter (ADC), as is are the anode wires which are all ganged together.

A MWPC back window is used to isolate the scintillator from the wirechamber gas (neopentane), In order to minimize the backscattering effect, a very thin mylar film is used as the back window. This mylar film is at present 25μm for the commissioning of the SCS, but in the final experiment, this exit film will be only 6μm. The wirechamber gas pressure is 100 Torr, thus the scintillator detector is isolated in a nitrogen gas volume with about 100 Torr of pressure. A gas handling system protects the wirechamber windows while pumping, filling, or venting the system.

The scintillators are 3.5 mm thick, 15 cm diameter plastic scintillators. (The range of 782 keV betas in plastic scintillator is 3.1 mm. Allowing for a small safety factor sets the scintillator thickness to be 3.5 mm.) We use Bicron BC-400 scintillator that has a light output of 65% of anthracene, and a 2.4 ns decay constant, and an attenuation length of 250 cm. The scintillators are coupled to 4 light pipes that are approximately 40 cm long, which come out in the direction of the plane of the scintillator at 90^{o} to each other. The ends of these light guides are mated to 50 mm diameter fast (3 ns rise time, 4 ns FWHM) photomultiplier tubes, PMTs (RCA 8850). An optical fiber is connected to the scintillator in order to allow an LED pulser signal to be fed into the scintillator package for use in the PMTs' gain stabilization. Requiring a coincidence between

at least two of the PMTs greatly reduces the noise due to dark current. With the specified background noise rate of 5 kHz for these PMTs, using a 10 ns coincidence window between two PMTs results in a residual noise rate of only 0.25 Hz.

The PMTs are in a fringe field of the solenoid magnet of order 500 Gauss. The PMTs have a sensitivity to magnetic fields of a reduction in output amplitude by 50% in a field of 3 Gauss along the axis of the PMT and of 1-2 Gauss (depending on orientation) for fields transverse to the PMT axis. To achieve 98% of the zero-field output amplitude, we need to reduce the fringe field to about 400 mGauss. This is achieved using soft iron shields, Mu metal shields and bucking coils which produce a magnetic field in the opposite direction of the fringe fields along the PMT axis.

One of the major sources of background is cosmic-ray muons. The muon rate at LANSCE altitudes is about 0.016 Hz/cm^2 and has an angular distribution of $\cos^2\theta$ (where θ is the angle with respect to a vertical axis). The muons directly produce a signal both in the proportional counters and the scintillators. However, as they typically have an energy greater than 1 GeV, they produce continuous ionization across the entire path in the scintillator and typically leave more than 1 MeV of energy deposited in the scintillator. They also typically traverse the wire chambers at large angles and thus can be identified by their large □E. The estimated rejection efficiency is > 95%. To further identify cosmic-ray muons from betas, we have begun to install scintillator vetoes in and around our detector system. Both east and west detectors now have a backing veto which sits behind the beta scintillator and identifies muon events which traverse the detector perpendicular to the plane of the beta scintillator. Before the December 2005 beta-decay run, we constructed and installed a top veto, which is a huge scintillator paddle that sits on top of the detector system. This veto is meant to identify muon events that traverse the detectors from above. Eventually, there will be a top, and two side panels for both sets of detectors. (UCNA Collaboration)

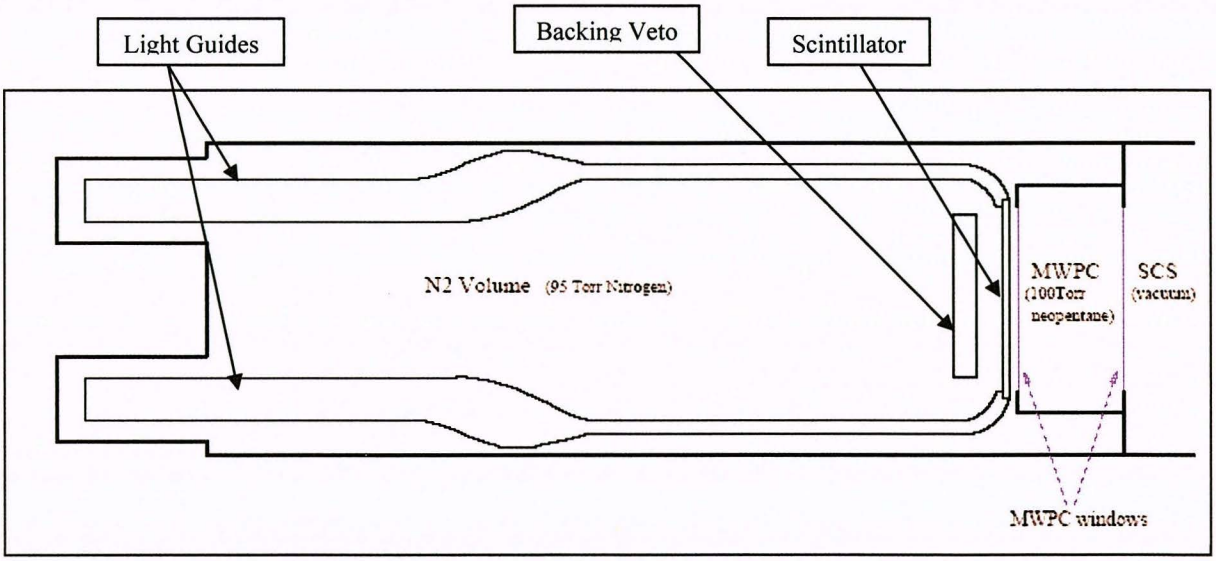

Figure 3 Overview of detector system

Experimental Procedure

Dec '05 Beta-decay Run

In December 2005, we performed a 61-hour long beta-decay run. For this run, there was a switcher in the guide tubes between the PPM and the AFP magnets which could switch the neutron beam from going straight into a neutron bottle which was being used to measure the lifetime of the neutron, to going into the SCS for beta-decay measurements. Switcher "on" indicates that the neutrons are guided to the SCS, while switcher "off" means they are guided to the neutron bottle. During this run, the superconducting spectrometer (SCS) was held at 0.5 Tesla. A 2 meter long decay trap with copper coated Kapton windows at the ends was installed and operational, as was the east beta-detector package (including the MWPC and scintillator), the east backing veto, and the top veto. A silicon detector from the University of Washington was also installed, but was only operational near the end of the run. Of note, a boron (^{10}B) foil from the UW silicon detector was exposed to UCN flux at the west end of the decay trap.

After examining some of the data taken, we noticed an excess of rate at energies from ~700-800 keV (see figure 4). In the runs (only 2) taken during an October 2005 beta-decay run, there was essentially no evidence for any excess rate over background. Thus, this noticeable excess was not expected and could not be taken as beta-decay. By looking online at the rates while the data was coming in, we could see that it took some time (< 5 minutes) after the beam was turned on for this excess rate to accumulate. There were only small differences in the configuration of the hardware between October and December. One was that new guides had been installed in the switcher; it is unlikely that they would produce a new signal in the beta-detectors. Two was that the SCS was held at 0.5 Tesla instead of 1.0 Tesla; again, it is unlikely that this would be the cause of excess signal. However, the third change, the UW silicon detector with the ^{10}B foil exposed to UCN flux, might have been the cause.

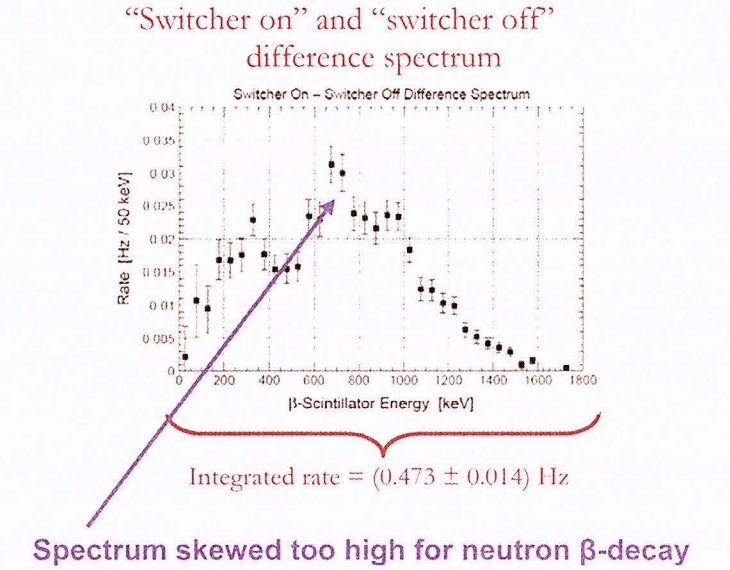

Figure 4 Search for neutron beta-decay by comparing rates between switcher "on" and switcher "off." We find an excess in rate from ~700-800 keV.

It turns out that the evidence shows that the ^{10}B was not the cause of the excess, but that the Al foil holder which was holding the ^{10}B foil in place was the cause. Following activation by thermal neutron capture, ^{28}Al decays (100%) to the 2^+ state of ^{28}Si via beta-decay along with the emission of a photon. This has an end-point energy of 2.87 MeV; the photon energy is 1.78 MeV, and the mean electron energy is ~1.25 MeV. The lifetime of this process is 3.23 minutes, which is approximately how long it took for the excess signal to accumulate. Unfortunately, since it was shown that the beta-decay rates were swamped by the Al beta-decay rates, we decided not to further analyze these runs.

Jan '06 Beta Detector Calibration Run

In January 2006, we performed an 80.2 hour (3.3 day) long beta detector calibration run. During this run, the SCS volume was sealed off by blanking off the entrance window to the SCS. The superconducting magnet was held at 1.0 Tesla for the entire run, and the decay trap was removed from the bore of the spectrometer. Both east and west detector packages (MWPC, scintillator, and backing veto) were installed and operational, with an additional top veto on the east side. Of the 80.2 hours, the DAQ ran for 28.5 hours; down time was due to venting/filling the gas volumes in order to switch out the source holder, SCS liquid He refills, detector debugging, and to fix the back window on the east MWPC.

One of the main goals of this experiment is to determine the position resolution of the detector systems. Thus, before the run began, the source holder was machined to the correct dimensions, and the position translator system assembled and carefully calibrated. The position translator system is composed of a brass bellows system coupled to a stainless steel tilt-a-port, both vacuum feedthroughs; the system was arranged so that the bellows provide horizontal translation (up to 15 cm when fully extended), while the tilt-a-port provides vertical angular motion (manufactured by HML to provide 10 degrees, but this motion is restricted by the aluminum rod within the narrow insides of the bellows). The bellows work by turning a dial on the end of the bellows to extend and retract the bellows inside. The tilt-a-port uses a micrometer to determine the degree of tilt (1mm = 1.2°, according to HML). The disk-like source was clamped down with the source holder connected to the end of a long aluminum rod (69 cm), which was firmly attached to the end of the bellows. Essentially, the tilt-a-port provided a tilt for the bellows which was in turn attached to the rod holding the source. This then allowed the source to sweep out a two dimensional area, including the fiducial area (plus 1.5 cm outside of the fiducial circle) that we wanted to test with our sources.

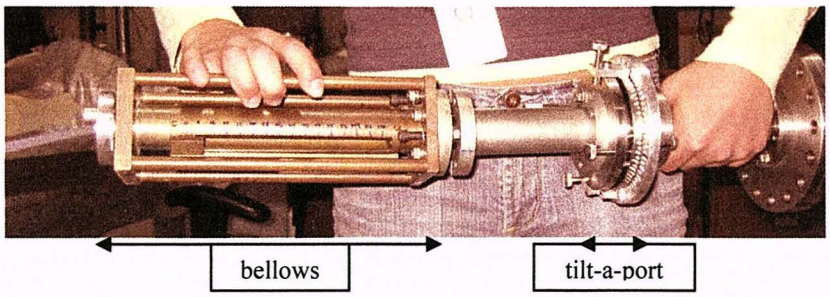

Figure 5 Brass bellows and tilt-a-port system

Before assembling the source holding system, the source holder had to be machined down to 6.3cm so that it could fit diagonally through the rectangular exit port of the SCS, which had a diagonal length of 8cm (with the addition of the radius of the aluminum rod, and the radius of the source itself, this was a tight fit). The aluminum rod also had to be shortened to 69cm so that it would fit within the diameter of the SCS bore when the bellows are fully extended.

After assembling the source holding system to the bellows and tilt-a-port, the entire system was installed onto the exit port of the SCS. A transit was then used to center the source within the SCS bore. It was determined that because of the dimensional limitations of the exit port and the limitations of the tilt-a-port, in order to cover the entire fiducial area (5 cm radius) plus an additional buffer zone of 1.5 cm outside the area, it would require three different configurations of the source holder on the aluminum rod. These three configurations are shown in figure 8. After centering the source in the SCS volume, the system was uninstalled and calibrated for position outside of the SCS. This was done since it was extremely difficult to determine position information while the source was in the center of the SCS.

We could not just measure a few positions and extrapolate for all the other positions since the source motion was restricted by the movement of the rod inside the feedthroughs, which made the positions very non-linear. It was also more accurate to measure all the positions on an approximately 1cm by 1cm grid since the weight of the aluminum rod and the source also factored into the ultimate position of the source. Each grid point was measured as the number of turns on the bellows dial versus the tilt value given by the micrometer on the tilt-a-port. These values were later converted to actual length values, as shown in figure 6. The center of the SCS was defined as $x = y = 0$ (or, 51 turns, 11.50mm tilt). These positions were measured to within ±3mm of the actual position. We call these position values the "nominal" positions.

We had wanted to determine whether pumping on the SCS system down to vacuum would affect the absolute position of the source. However, there was no viewing port which could allow us to see that affect through the transit. There are some systematic effects on the nominal positions that we detect in the data analysis, and which will be discussed later.

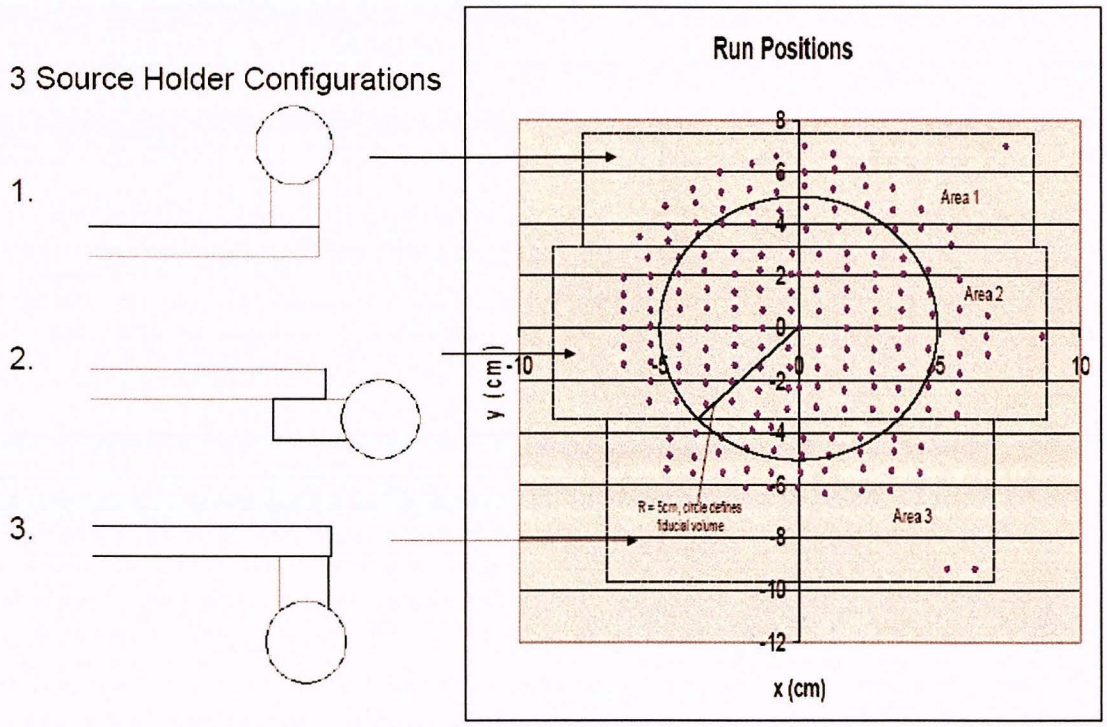

Figure 6 Source holder configurations and positions mapped out over runs. Each source holder configuration corresponds to an area of the map. The fiducial area is defined by the 5cm radius circle.

Before starting any of the runs, we assessed the baseline voltages of all the MWPC cathode wires. (We discard channels 1 and 16, using only channels 2 through 15). All the cathodes on the east side were fine (had positive baselines), but there were a few on the west side which had highly negative baselines (< -100 mV). The "bad" channels were padc9, padc12, padc19, and padc30. The baseline voltage is the noise in the detector when there are no events triggered in the detector. This, and the baseline voltages from the electronics translate to a pedestal signal in our data spectra. Sure enough, when we started taking data, the "bad" channels either had a signal which was indistinguishable from the pedestal, or no signal at all. This issue will be further addressed in the data analysis.

Channel	E vertical (mV)	E horizontal (mV)	W vertical (mV)	W horizontal (mV)
1	-80	nothing	-52	nothing
2	44	336	-194	216
3	132	648	190	-104
4	16	680	180	-20
5	444	452	-108	28
6	56	452	212	50
7	224	172	216	-42
8	-88	172	168	-96
9	-8	172	-42	-252
10	104	40	18	-72
11	176	320	360	-28
12	204	120	-272	100
13	144	296	22	2
14	56	156	8	-174
15	224	440	-5	132
16	nothing	nothing	-292	-76

Table 1 Baseline voltages for MWPC cathode wires

At the beginning of the run, the following high voltage settings were determined for the detector hardware so that the gains between the PMTs would roughly match:

PMT 1E HV	1975 V
PMT 2E HV	1950 V
PMT 3E HV	2025 V
PMT 4E HV	2025 V
PMT 1W HV	2050 V
PMT 2W HV	2050 V
PMT 3W HV	2000 V
PMT 4W HV	2150 V
E bucking coil current	0.30 A
W bucking coil current	0.20 A
E backing veto HV	2300 V
W backing veto HV	2300 V

Table 2 Hardware HV/current settings for first half of runs

Table 3 is a summary of the first half of the runs we took (this first set of runs was taken without having to vent the system):

Run #	Description
2309-2315	^{113}Sn source in configuration #2, energy calibration runs (at the center for ~1.75 hours and at 6 surrounding positions for ~30 minutes each); note: east MWPC anode was not working properly (see figure 9); estimated source rate: 40 Hz
2316-2424	^{113}Sn source in configuration #2, position calibration runs, each 2 minutes, east anode would work only sporadically
2425	~2.25 hour background run with ^{113}Sn source completely outside of the

	fiducial area (we saw no electron events)
Vent and Break	Fixing E MWPC back window (~1.6 days)

Table 3 Summary of first half of runs

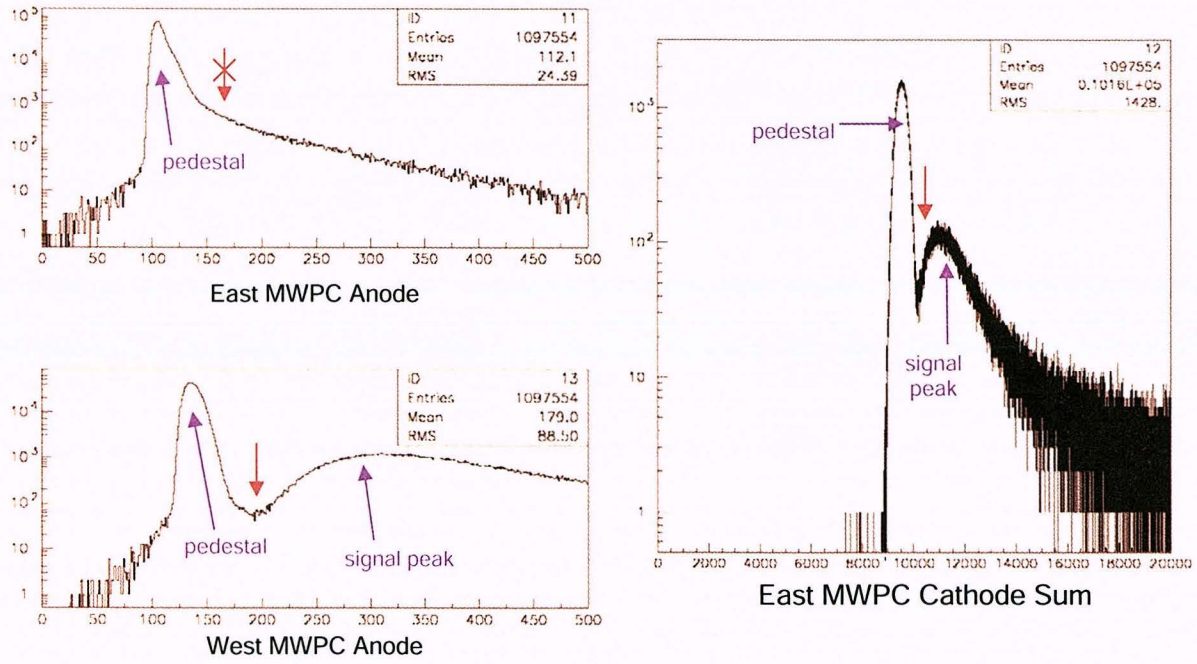

Figure 7 East MWPC anode (with no visible signal peak); West MWPC anode shows clear separation between pedestal and peak; East MWPC cathode sum shows clear separation between pedestal and peak, and so can be used in analysis in place of the East MWPC anode.

As shown in figure 7, the east anode was not working properly; there was essentially no signal registering. Sporadically throughout all the runs, the east anode would work, but it was not reliable, and would often stop working in the middle of a run. In order to still be able to require coincidence between the MWPC and scintillator, we determined that it would be feasible to use the east cathode sum as a replacement spectrum for the east anode – there is a distinct separation between the pedestal and signal in the east cathode sum, as shown in figure 7.

The reason we had to break for so long after the first set of ^{113}Sn runs was because after we had vented the system and were ready to begin the ^{207}Bi energy calibration runs, we noticed that there was a gas leak in the east detector package. We were able to narrow it down to a leak in the wire chamber back window since the window could not hold the slight pressure difference set between the MWPC neopentane volume and the scintillator N2 volume by the gas handling system. We were forced to create and install a new back window, which required 12 hours of curing for the glue to set. Normally the window is made using 6μm Aluminized Mylar film, but here we used 25 μm Mylar film so that it would be tough enough to sustain the cycles of venting and pumping of the system we had planned to do in the rest of the runs. This process required ramping down the main solenoid, venting of the SCS system, and since it was the back window which was leaking, we also had to take apart all the MWPC electronics, shown in figure 8 to replace the window.

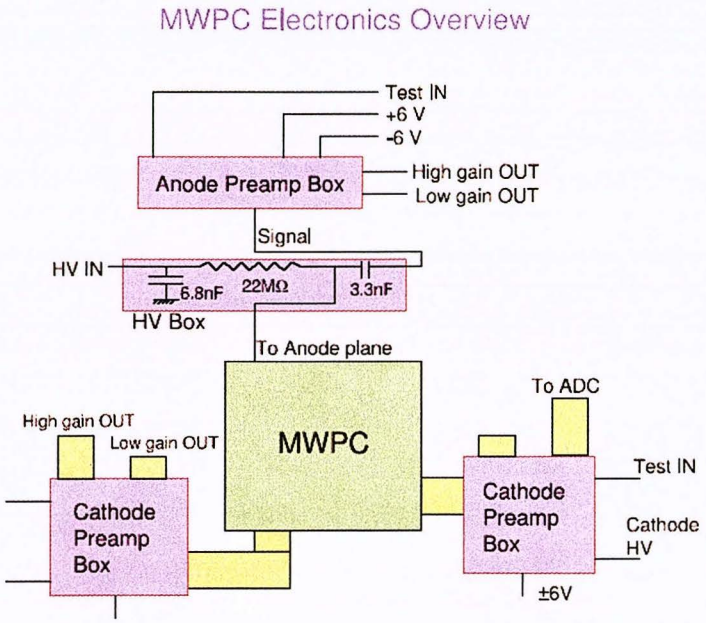

Figure 8 Schematic of MWPC electronics

PMT 1E HV	1975 V
PMT 2E HV	2000 V
PMT 3E HV	2075 V
PMT 4E HV	2025 V
PMT 1W HV	2050 V
PMT 2W HV	2050 V
PMT 3W HV	2000 V
PMT 4W HV	2250 V
E bucking coil current	0.30 A
W bucking coils #1-3 current	0.20 A
W bucking coil #4 current	0.35 A
E backing veto HV	2300 V
W backing veto HV	2300 V

Table 4 Hardware HV/current settings for second half of runs

Table 4 is a list of the high voltage and current settings for the second half of the runs. Note: the bucking coils on both the east and west sides began shorting to the mu-metal shields. We were able to fix all the bucking coils on the east side and most of them on the west side by adding electrical tape to the outside of the bucking coils. However, there was one on the west side which we could not fix, #4, and which had a noticeably lower PMT signal gain than the rest of the PMTs (the peak for #4 was at 1650 vs. 2000+ for the other PMTs). We thus decided to decouple bucking coil #4 from the other three, and set its current to be 0.1 Amps higher. Table 5 is a summary of the second half of the runs we took:

Run #	Description
2445-2455	^{207}Bi source in configuration #2, facing west, energy calibration runs (at the center and at 6 surrounding positions for ~23 minutes each); estimated source rate: ? Hz
Vent and Pump	
2456-2462	^{207}Bi source in configuration #2, facing east, energy calibration runs (at the center and at 6 surrounding positions for ~23 minutes each); estimated source rate: ? Hz
Vent and Fill	
2466-2508	^{113}Sn source in configuration #1, position calibration runs, each 2 minutes (but if the source were next to the edge of the fiducial area, then we ran for 8 minutes), east anode would work only sporadically
2509-2510	^{113}Sn source in configuration #1, ~1 hr long energy/backscattering runs
2511-2512	^{113}Sn source in configuration #1, ~1 hr long background runs with source completely outside of the fiducial area (we saw no electron events)
Vent and Fill	
2514-2549	^{113}Sn source in configuration #3, position calibration runs, each 2 minutes (but if the source were next to the edge of the fiducial area, then we ran for 8 minutes), east anode would work only sporadically
2551-2554	^{113}Sn source in configuration #3, ~1 hr long background runs with source completely outside of the fiducial area (we saw no electron events)

Table 5 Summary of second half of runs

Data Analysis

Scintillator Position Analysis

One systematic error that we noticed in the data analysis is that all the nominal y positions which correspond to runs taken with the source holder in the 3rd configuration were all too low, by an average of 2.7cm in the scintillator, and 1.7cm in the wire chamber. Such a large offset may have occurred if the long rod was rotated in its socket while we were installing the bellows/tilt-a-port in the SCS. This would create an offset in y, but not one in x. The nominal y positions which correspond to runs taken with the source holder in the 1st and 2nd configurations were high, by an average of 0.2cm in the scintillator, and 1.3cm in the wire chamber. The nominal y positions are thus all adjusted for this offset before we start the analysis.

Another one of the first steps in the data analysis was to write a Physics Analysis Workstation (PAW) kumac to extract the pedestal positions from each scintillator qadc (charge-integrating ADC) signal, and for all the anode/cathode padc (peak-sensing ADC) signals. This was done by searching the entire spectrum for the highest channel (the pedestal is always higher than the signal, and so it is the highest peak in the spectrum), and then fitting a Gaussian around that peak value. Both the mean and sigma values were saved from those fits. In the Appendix, chart 1 matches each DAQ variable name to what it is measuring. Figure 9 is a plot of the individual scintillator PMT (qadc) pedestals vs. time, where the mean run time is the mean absolute time of each run. As can be seen, the PMT pedestals are relatively stable, many not varying by more than a few channels, and some varying by ~ ± 5 channels. The pedestals for the wire chamber will be shown in the next section.

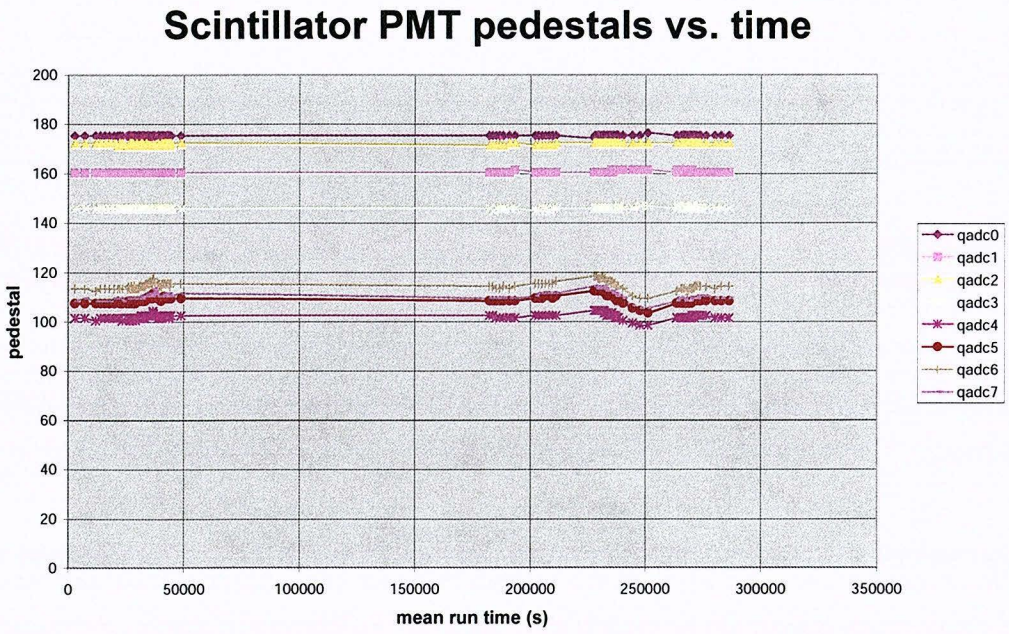

Figure 9 Plot of individual scintillator PMT pedestals vs. time

After the pedestals were determined, a kumac was developed to extract the signal pulse height for each qadc from each run. This was accomplished in a similar fashion to the pedestal program, except that now the pedestal peak was subtracted from the spectra so that the pulse height would be the highest peak in the spectra. These pulse heights are then averaged over the entire run, as opposed to extracted event-by-event. We will develop an event-by-event analysis of the data, as described later.

Before we make theoretical corrections to the experimental data though, we adjust the pulse heights according to shifts in gain during all the runs. Theoretically, as long as the source is within the fiducial area, the qadc sum pulse height should remain the same over all the runs. Thus, we use the qadc sum to correct for drifts in gain. Figure 10 shows the drift in gain in the east PMTs over time. From this plot, it seems as though there are different linear corrections to the gain based on which set of runs (before or after fixing the east MWPC back window) we are considering. We correct every run shifting its gain back to the level of the very first run. Thus, we fit the two sets of runs separately with linear fits. The first set of runs can be adjusted by a multiplicative factor based on this linear fit. The second set of runs, however, must first be adjusted multiplicatively to have the same baseline value as the first set of runs, and then we apply the multiplicative linear fit factor. Essentially, the second set of runs is moved up to the same mean gain level as the first set, and then we remove the slope in time of the gains.

The difference between east/west sum and sum east/west qadc pulse height values is that the east/west sum is derived from my kumac program as a fit of the qadc sum spectra, whereas the sum east/west value is just the sum of the individual qadc pulse height values taken from the kumac.

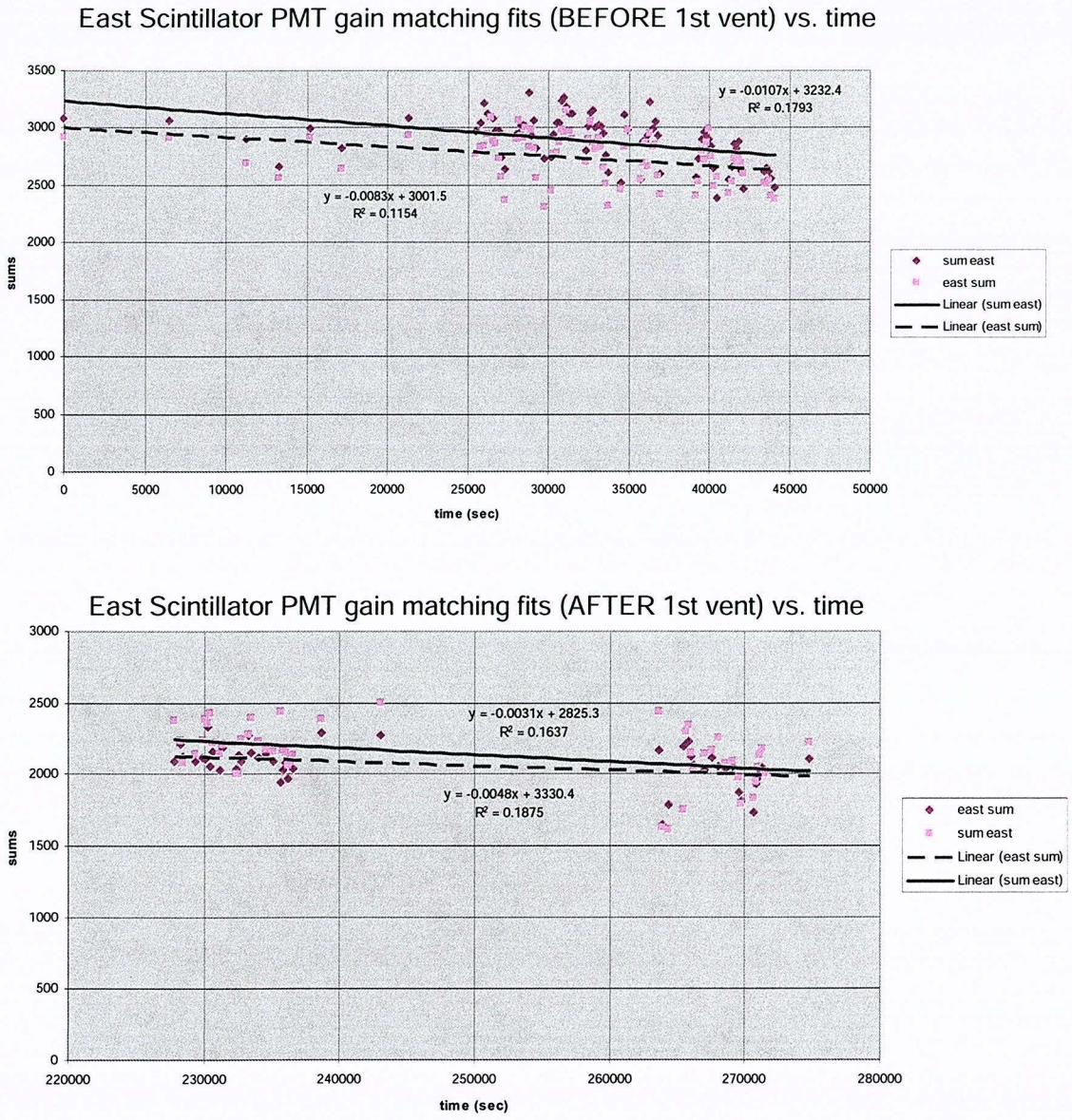

Figure 10 Linear Fit Plots of Scintillator PMT gains before and after the first vent.

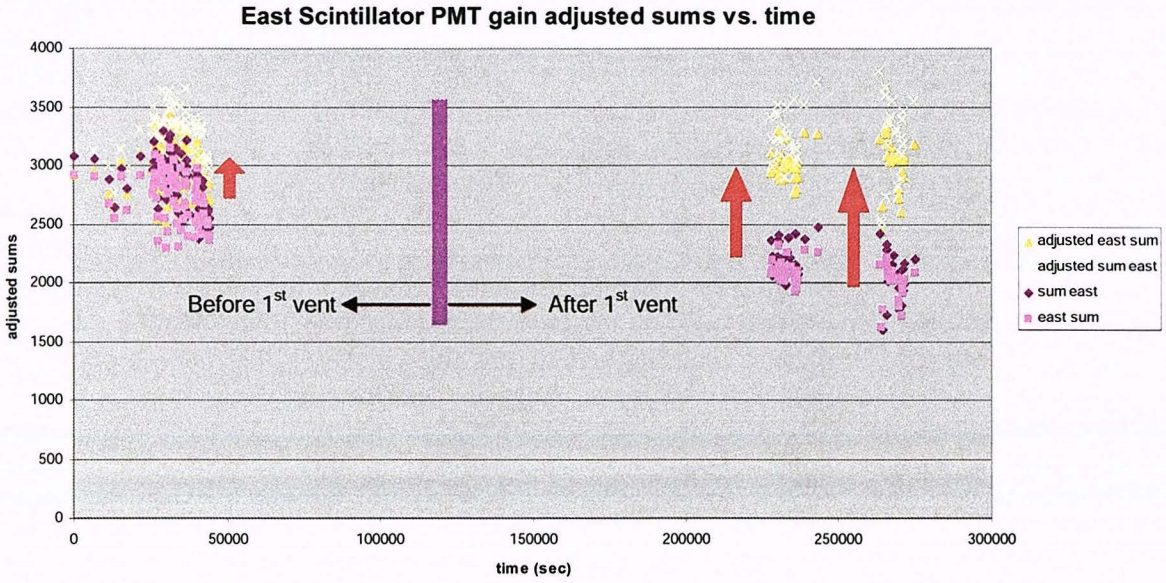

Figure 11 East Scintillator PMT gain adjusted values over time (purple and blue indicate gain values before the gain adjustment; teal and yellow indicate gain values after the gain adjustment)

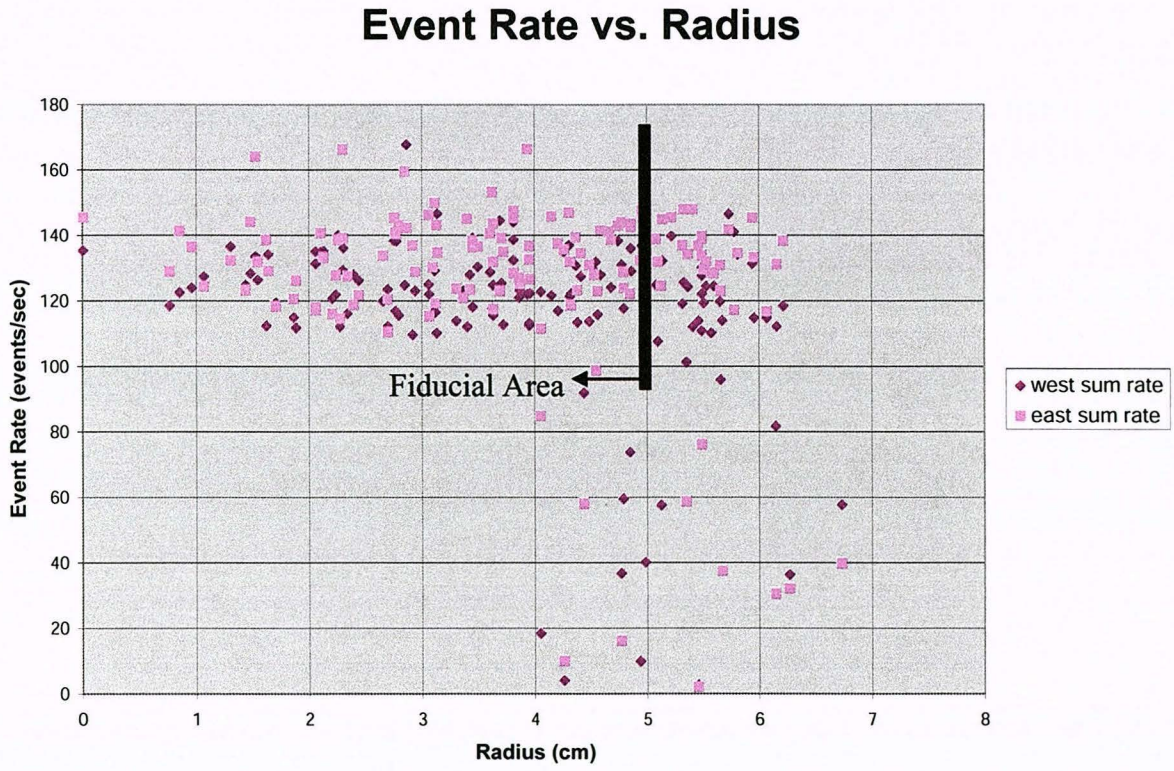

Figure 12 Event Rate vs. Radius in ^{113}Sn signal peaks.

After adjusting all the gains, we wanted to see how the rate is correlated with the position of the source in the spectrometer. The rate is determined by summing the number of events in the ^{113}Sn signal peaks, and dividing that sum by the length of the run in seconds. As we can see in figure 21, a plot of the event rate versus radius, most of the events in the fiducial area (within a nominal radius of 5cm) have a decent event rate of about 110 events/sec. However, as we go outside of the radius of 4cm, we begin to see a few runs where the event rate drops below 100 events/sec. This would occur if in fact nominal positions of the source actually fall outside the fiducial area. We see evidence in the position data below that the magnetic field itself may be tilted in the x plane so that the electrons spiral towards a more negative x position in the east detector, while spiraling towards a more positive x position in the west detector. Essentially, the horizontal axis of the spectrometer bore and the axis of the field are not aligned. There does not seem to be any field tilt in the y direction. Thus, if the source is somewhat near the edge of the fiducial area, one detector will register that it is outside the area while the other will register that it is well within the fiducial area. We believe that is what gives rise to the drop in some of the event rates. Using the event rate is an efficient way to determine the edge of the fiducial region. Correcting for this tilt in the field axis is an item for more detailed analysis.

It is important to be able to determine the event position from the scintillator to a reasonable resolution so that we are able to double check the values given from the wire chamber. In determining the position from the scintillator, we developed theoretical calculations of what the PMT signals would register, given a particular (x, y) point on the scintillator surface. The radius of the scintillator is in reality 7.5 cm. However, I chose to reference every position to the position of the source at the center of the spectrometer, which is at 1 Tesla, whereas the scintillator is in a 0.6 Tesla field region. The conversion from one field strength to the other is the square root of the ratio between the field strengths. Thus, in calculating the PMT signal strengths, I take the radius of the scintillator to be: $\sqrt{(0.6)} * 7.5\ \text{cm} \approx 5.8\ \text{cm}$. From the Law of Cosines, we can easily determine the angles α, β, γ, and δ from figure 13, which we assume to be directly proportional to the pulse heights of the qadc's (here labeled q1, q2, q3, and q4, where $Q=\sum$ qi's). The formulas include IF statements because once the angle exceeds π (occurs when the x, y point exceeds the diagonal line between the two points around that particular quadrant where the circle crosses the horizontal and vertical axes), the geometry assumes that we are calculating the inner angle, as opposed to the desired outer angle. We must then solve for the complement of what the geometry gives.

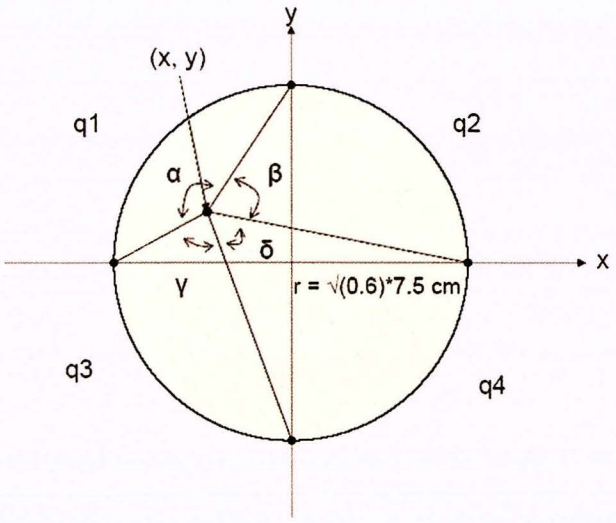

$$\alpha[x\_, y\_] := \text{If}\left[y \le r+x,\ \text{ArcCos}\left[\frac{y^2+(r+x)^2+(r-y)^2+x^2-2r^2}{2\sqrt{(r-y)^2+x^2}\ \sqrt{(r+x)^2+y^2}}\right],\right.$$

$$\left.2\pi - \text{ArcCos}\left[\frac{y^2+(r+x)^2+(r-y)^2+x^2-2r^2}{2\sqrt{(r-y)^2+x^2}\ \sqrt{(r+x)^2+y^2}}\right]\right]$$

$$\beta[x\_, y\_] := \text{If}\left[y \le r-x,\ \text{ArcCos}\left[\frac{y^2+(r-x)^2+(r-y)^2+x^2-2r^2}{2\sqrt{(r-y)^2+x^2}\ \sqrt{(r-x)^2+y^2}}\right],\right.$$

$$\left.2\pi - \text{ArcCos}\left[\frac{y^2+(r-x)^2+(r-y)^2+x^2-2r^2}{2\sqrt{(r-y)^2+x^2}\ \sqrt{(r-x)^2+y^2}}\right]\right]$$

$$\gamma[x\_, y\_] := \text{If}\left[y \ge -x-r,\ \text{ArcCos}\left[\frac{y^2+(r+x)^2+(r+y)^2+x^2-2r^2}{2\sqrt{(r+y)^2+x^2}\ \sqrt{(r+x)^2+y^2}}\right],\right.$$

$$\left.2\pi - \text{ArcCos}\left[\frac{y^2+(r+x)^2+(r+y)^2+x^2-2r^2}{2\sqrt{(r+y)^2+x^2}\ \sqrt{(r+x)^2+y^2}}\right]\right]$$

$$\delta[x\_, y\_] := \text{If}\left[y \ge x-r,\ \text{ArcCos}\left[\frac{y^2+(r-x)^2+(r+y)^2+x^2-2r^2}{2\sqrt{(r+y)^2+x^2}\ \sqrt{(r-x)^2+y^2}}\right],\right.$$

$$\left.2\pi - \text{ArcCos}\left[\frac{y^2+(r-x)^2+(r+y)^2+x^2-2r^2}{2\sqrt{(r+y)^2+x^2}\ \sqrt{(r-x)^2+y^2}}\right]\right]$$

$$q1[x\_, y\_] := \frac{Q}{2\pi}\,\alpha[x, y]$$

$$q2[x\_, y\_] := \frac{Q}{2\pi}\,\beta[x, y]$$

$$q3[x\_, y\_] := \frac{Q}{2\pi}\,\gamma[x, y]$$

$$q4[x\_, y\_] := \frac{Q}{2\pi}\,\delta[x, y] \qquad Q := \sum_{i=1}^{4} qi$$

Figure 13 Theoretical calculation of the signals in each PMT (directly proportional to the angle created in that quadrant), based on a given (x, y) coordinate.

Unfortunately, as far as we know, these formulas are not invertible; that is, we cannot determine real unique (x, y) values given q1, q2, q3, and q4 values. There does not seem to be an analytical solution to this problem (it would be possible to create a lookup table of values which would convert the qi's into (x, y) pairs).

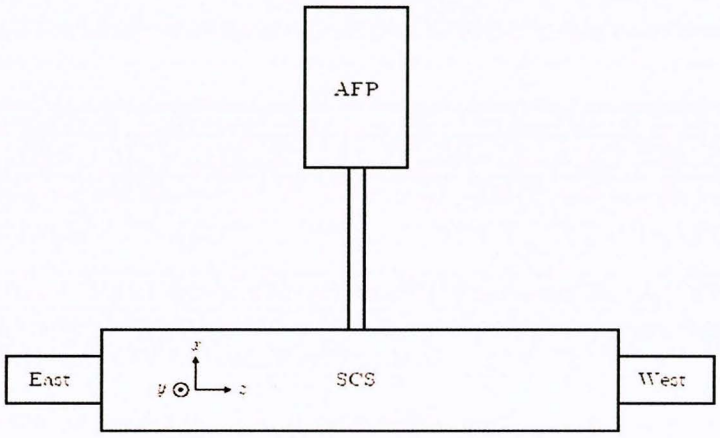

Figure 14 Analysis coordinate system

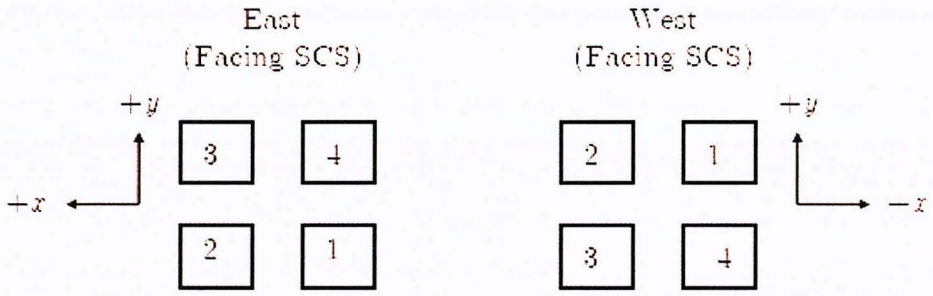

Figure 15 PMT arrangement with coordinate axes

We decided to pursue a different approach which avoided using a lookup table to determine the (x, y) values – creating the lookup table requires the choice of grid size which ultimately biases the resolution analysis of the detector. Instead, we chose to use a simple, but approximate calculation of the position which merely uses the difference between the sum of two adjacent quadrants and the sum of their opposite quadrants, normalized by the sum of all the quadrants, to determine the x and y positions, as the formulas show in figure 16. We shall call this the zeroth order calculation method, and call the other method the theoretical calculation.

$$x0 := 2r\frac{q2 + q4 - q1 - q3}{q1 + q2 + q3 + q4}$$

$$y0 := 2r\frac{q1 + q2 - q3 - q4}{q1 + q2 + q3 + q4}$$

Figure 16 Formulas for the zeroth order calculation of scintillator position.

Given (x, y) pairs, we can use the α, β, γ, and δ formulas to simulate qi's, and then calculate (x0, y0) pairs. We can then determine how far off the simple method is from the true (x, y) values.

We can see from the difference plots in figure 17 that as y increases, the simple method gives values which increasingly diverge from the true value of x. There are analogous plots for difference plots in y with varying values of x.

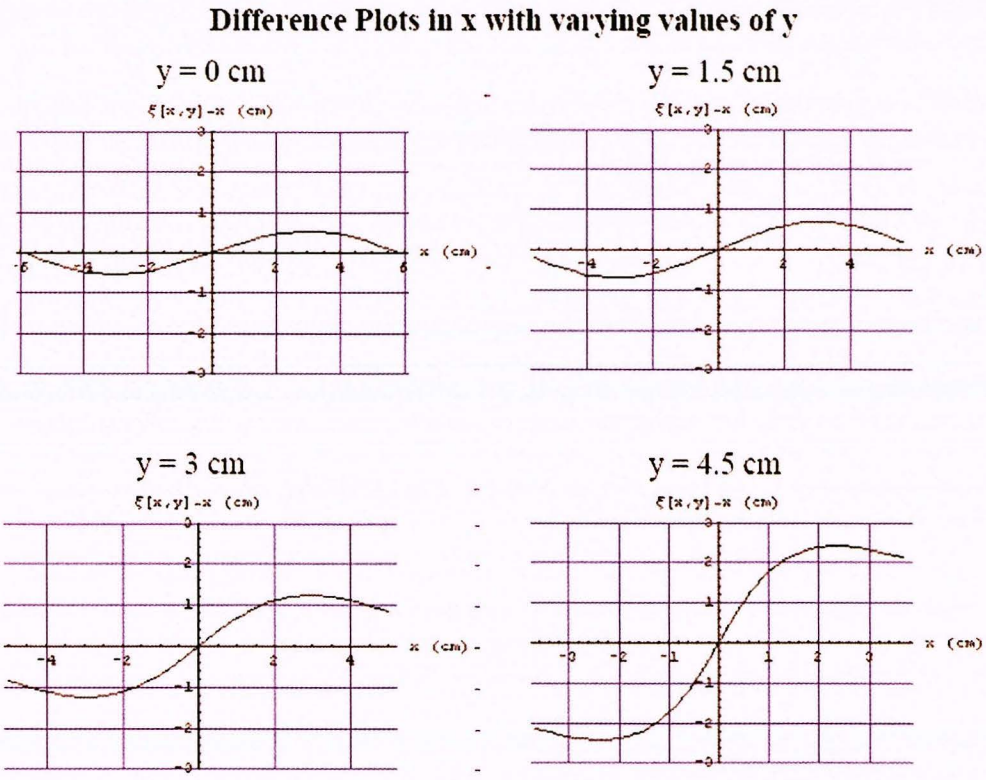

Figure 17 Difference plots in x with varying values in y

In determining the experimentally calculated positions, I use the run averaged qadc pulse heights (Gaussian fits of the signal peak to determine the pulse heights) to calculate the simple position values. When we plot the difference between the experimental values and nominal x and y values (source position values which I measured outside the SCS with the bellows/tilt-a-port system) versus nominal x and y, we see a similar pattern to the curves given by the theoretical difference plots (see figure 18), except that the experimental positions have tails at the extremes (large values of x and y) which re-cross the zero axis line.

One idea is to correct for these experimental differences by applying a correction based on the theoretical difference curves. Thus, we use the experimentally calculated zeroth order values of x0 and y0 as input values into the α, β, γ, and δ formulas to then generate new (xx0, yy0) pairs; the difference between the input (x0, y0) values and the (xx0, yy0) pairs would then be subtracted from the original input values. Since we always define the difference to be (calculated value – nominal value), this gives the final value:

$$\Delta x = xx0 - x0$$
$$x1 = x0 - \Delta x = 2\,x0 - xx0$$

$$\Delta y = yy0 - y0$$

$$y1 = y0 - \Delta y = 2\,y0 - yy0$$

The results of the correction are shown in figure 18. The first plot is the difference between the zeroth order approximation and the nominal position, x0-xn (note that it has the characteristic shape shown in figure 17 from the theoretical calculations). After correcting with the theoretical calculation, we see that the difference in positions flatten out in the region between -3.5 cm and 3.5 cm, but spread further from the nominal positions outside this region. The overall spread is due to the fact that all values of y are included in these plots.

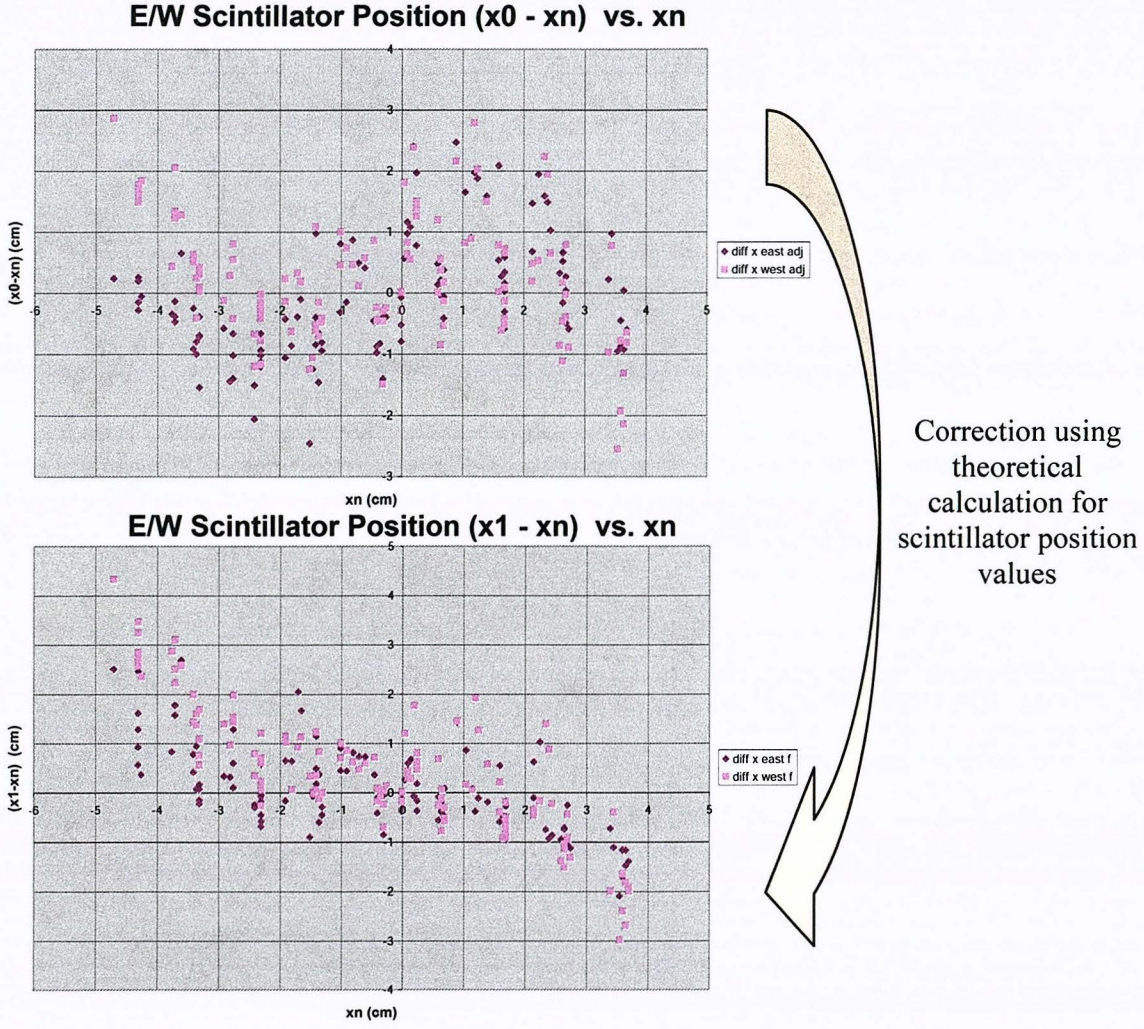

Figure 18 Scintillator position difference plots. First plot is the difference between the zeroth order approximation and the nominal position, x0-xn (note that it has the characteristic shape shown in figure 17 from the theoretical calculations). After correcting with the theoretical calculation, we see that the difference in positions flatten out in the region between -3.5 cm and 3.5 cm, but spread further from the nominal positions outside this region. The overall spread is due to the fact that all values of y are included in these plots.

The last step in the position reconstruction analysis for the scintillator was to determine a position resolution by examining event-by-event analyzed position spectra. This was carried out

using another kumac which used the same zeroth order formula to calculate the position from the scintillator PMT values. This created reconstructed position spectra like the ones shown in figure 19. The resolution in the event-by-event analysis was typically ~ .5 cm.

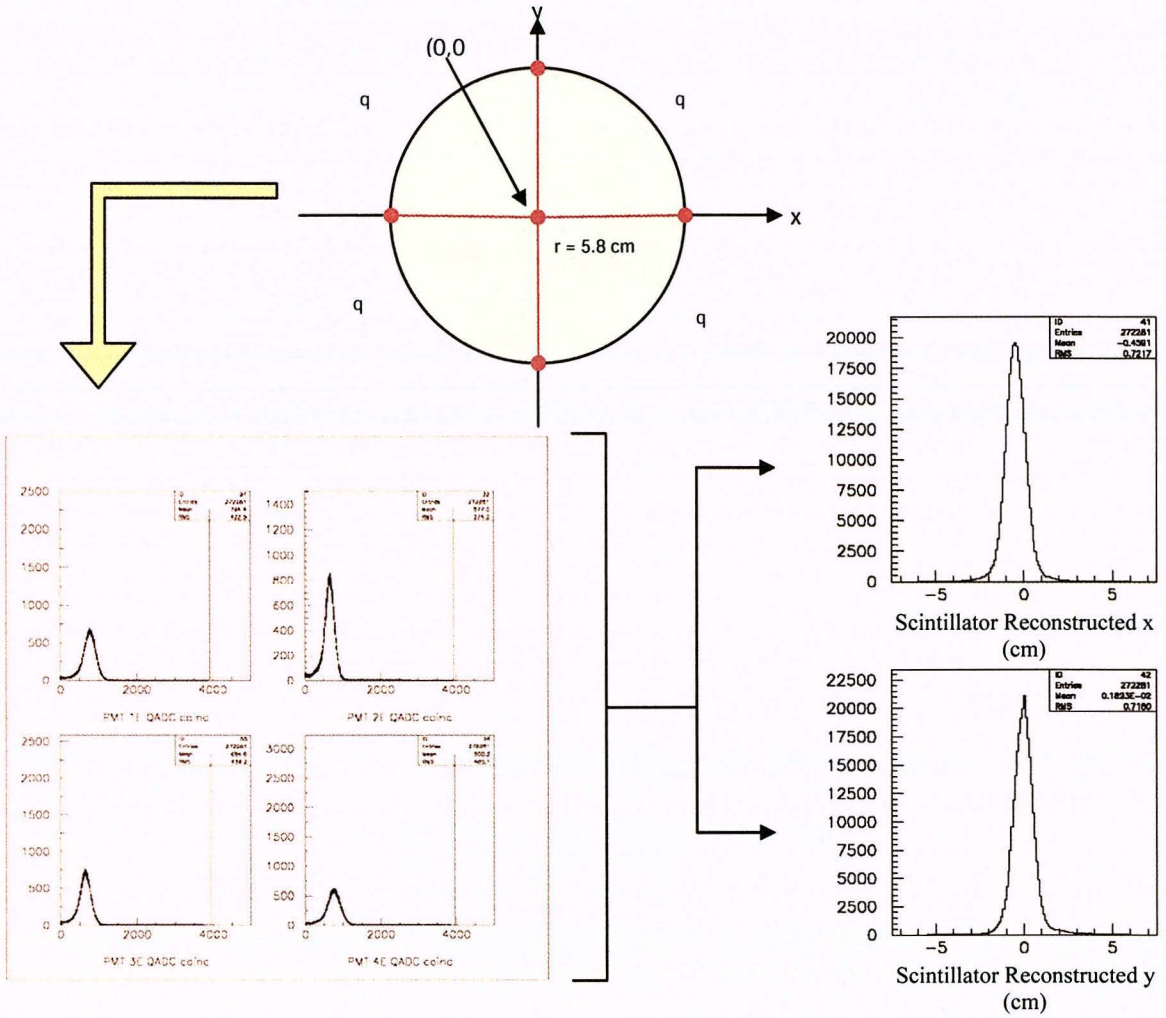

Figure 19 Scintillator position information calculated event-by-event with the zeroth order approximation from the 4 PMT signals give rise to x and y position spectra.

MWPC Position Calibration Analysis

Analogous position reconstruction analysis was performed for the wire chamber data. The pedestals for the wire chamber however are not as stable as those for the scintillator. This may be because the readout electronics for the MWPC are more sensitive to temperature fluctuations and other environmental fluctuations than the scintillator PMTs are.

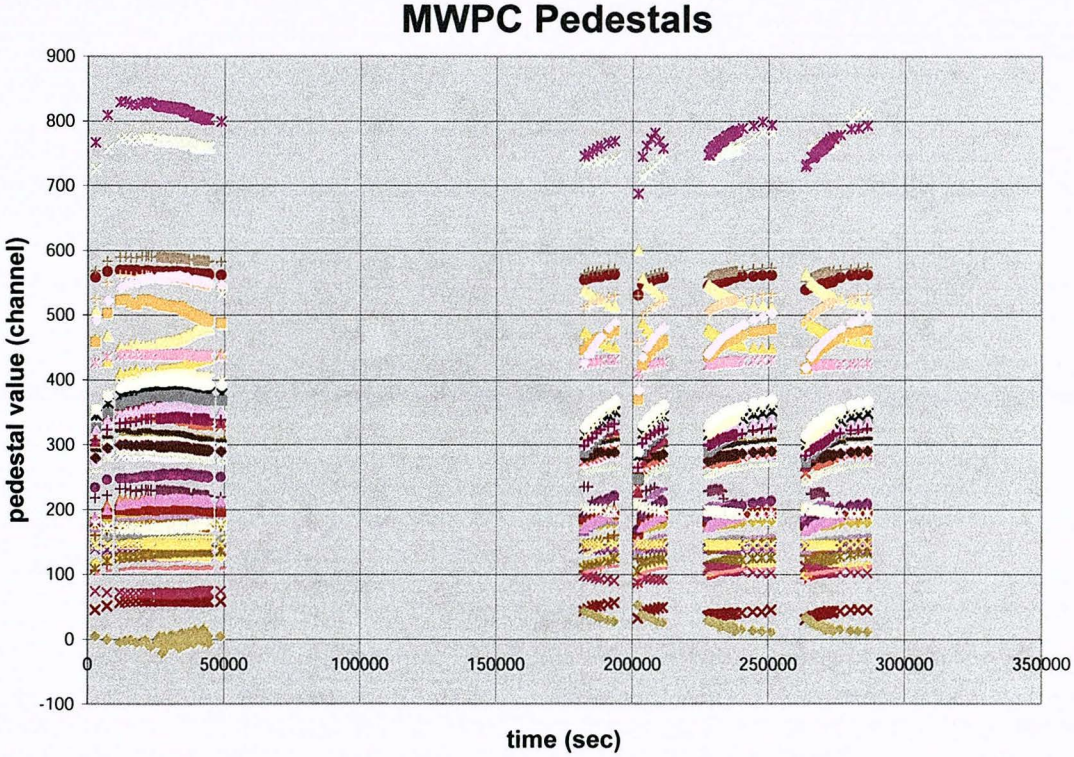

Figure 20 MWPC Anode/Cathode Pedestals (without the "bad" cathode channels)

When an electron strikes the anode plane, it induces a charge on the cathode wire planes. We want to calculate how many cathode wires should register a signal each time the detector is hit. This problem can be approximated by a point charge over an infinite conducting plane (the cathode wire planes and the anode are separated by only 1cm, while the plane is 15cm in diameter). From Purcell, we have that the surface charge density σ is given by the equation below, where r is the distance on the surface of the plane from the point charge, and h is the distance from the point charge to the plane. The full-width at half maximum is then ~1.53cm. Since the cathode wire bundles are spaced 1.016cm apart, this FWHM charge density covers the width of at least two wires, if not three. Thus, in the data, we can assume that there should be no single cathode wire firing alone, without an adjacent wire firing, in any event.

$$\sigma = -\frac{Qh}{2\pi (r^2 + h^2)^{\frac{3}{2}}}$$

$$\sigma_{\frac{1}{2}} = -\frac{Q}{4\pi h^2} = -\frac{Qh}{2\pi (r^2 + h^2)^{\frac{3}{2}}}, \quad h = 1\,\text{cm}$$

$$\Rightarrow r \approx 0.766421\ \text{cm}$$

$$\Rightarrow 2*r \approx 1.53\ \text{cm}$$

Figure 21 Calculation of full width half maximum radius of a charge 1cm above an infinite conducting plane. This is an approximation to the true problem of a point charge 1cm above a 15cm diameter conducting plane. We want to determine how many wires are expected to register a signal on the cathode wire plane in any given event.

Before determining the position from the wire chamber, we must discuss the "bad" channel baseline voltages we had observed earlier. The cathode channels which turned out to be "bad" in the data were all on the west side: padc9 and padc 12 (channels 9 and 12 on the x position-determining west cathode panel), and padc19 and padc30 (channels 3 and 14 on the y position-determining west cathode panel). To include these cathode signals in the position determination analysis would horribly bias the position values, but not to include them would also bias the resulting positions, especially for runs where the source is near that region of the cathode plane.

In the run-averaged analysis, we are able to correct for these "bad" channels by determining the amount of charge deposited on the cathode wires for a run where the source is not near any of "bad" channels. This is done by taking the fitted pulse heights for cathodes that fired ("firing" requires that the pulse height is above our threshold, as discussed below) and adding them together to get the summed pulse height (these values correspond to the amount of charge deposited in the wire chamber). This summed pulse height (880 on the west x-determining panel and 641 on the west y-determining panel, as determined from run #2309, where the source is at the center and so out of range of the "bad" channels) proved to be a stable value across runs for the amount of charge that could be deposited in any run. Thus, if there are channels with pulse heights above threshold adjacent to the "bad" channels, then it is assumed that the "bad" channels also had charge deposited on them. The signal for the "bad" channels is then corrected as the difference between the sum of the "good" channels above threshold and the summed pulse height. This method seems to give reasonable results for position information (the sigma in the run-averaged position values subtracted from the nominal positions is $\sim \pm$ 0.34cm).

Unfortunately, it is not reliable to use such a method for the event-by-event position analysis since we do not have a stable estimate for the summed pulse heights on an event-by-event basis. There is a statistical spread in the pulse heights from event to event, so that the method would not provide a consistent correction to the "bad" channels. In the event-by-event analysis, instead, we use the average of the two adjacent channels to the "bad" channel as the approximate pulse height for that channel. Fortunately, there are no two adjacent channels which are both "bad." This seems to give us somewhat reasonable results, but we suspect that it could also be the cause of some peculiar position results in the west y-determining panel. The shape of the y position spectra on the west side does not have the normal smooth Gaussian that we see in the other three

spectra. The peak seems to spike up and then decay exponentially down. We have not determined what the exact cause of such a spectrum is; this is an item for further research.

The following is the procedure we use to determine the position from the MWPC. In the data analysis, for all the runs, each cathode wire signal has its pedestal subtracted. The pulse height is then determined from the remaining spectra (for run-averaged analysis, the signal peak is fitted to a Gaussian and the mean is taken as the pulse height; for event-by-event analysis, the signal is that event's pulse height after subtracting the pedestal). Any pulse height below our threshold (50 channels), is set to zero. Below our threshold we do not trust that the value is a true signal – in run-averaged analysis, if there is no signal, the fit will often return a negative value for the peak since there is only the tail of the pedestal to fit. To determine the position resolution from the MWPC, a weighted sum over these pulse heights and their associated positions is calculated (positions are given in Appendix A). However, we do not include in the weighted sum any channels that seem to have fired on their own without an adjacent channel firing as well. Setting pulse heights that are below our threshold to zero also essentially eliminate them from affecting the weighted sum. This method should select only those adjacent channels which fired from a real event to be added into the position calculation.

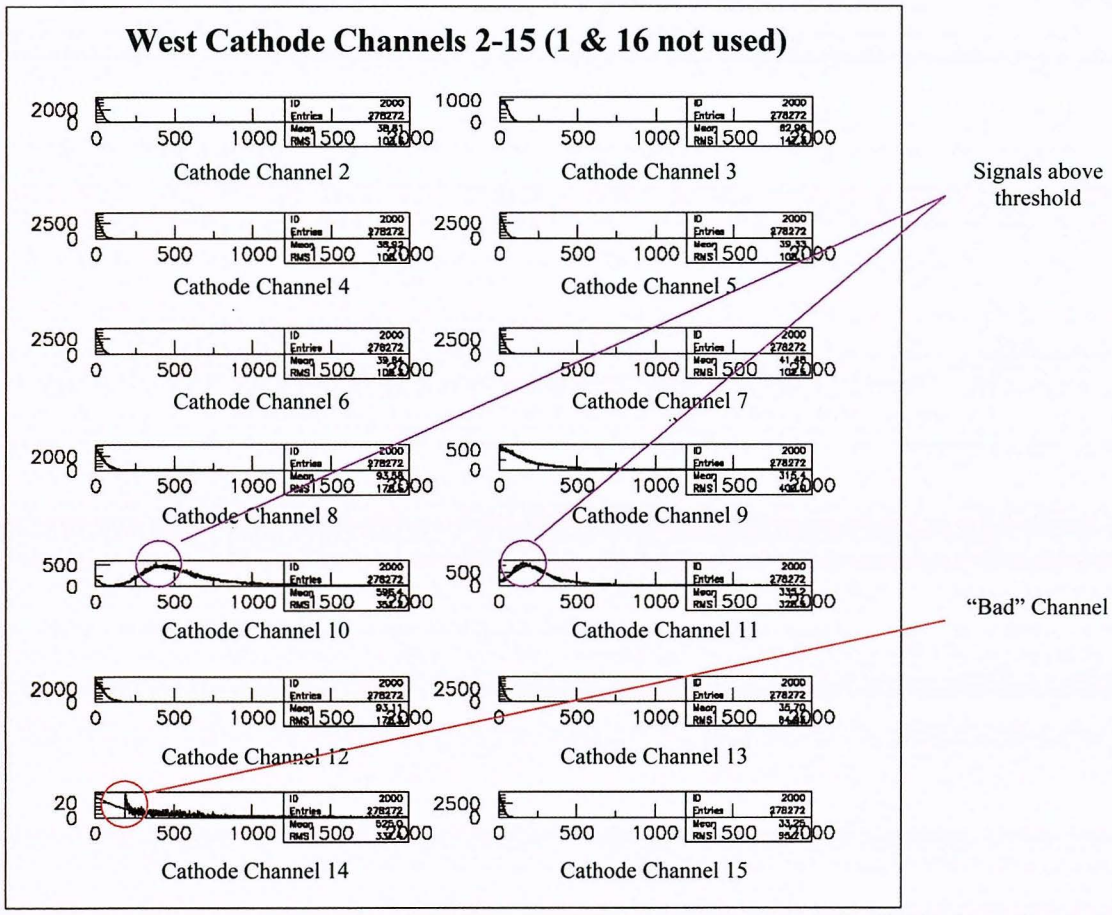

Figure 22 Example of channels with signals above threshold and an example of a "bad" channel spectrum. These are the type of peaks fitted in the run-averaged data analysis. Note: these spectra are pedestal subtracted.

The last step in analyzing the wire chamber data was to determine a 95% confidence upper limit on the fraction of events that are calculated to be at the wrong position (outside the main position peak). First, we can reduce the background by a factor of ~20 by applying a series of cuts on the data. Requiring a coincidence between the Sn113 events in the scintillator and the events in the wire chamber reduces background by a factor of ~10. Applying an additional cut on the backing veto (which is sensitive to cosmic ray events) further reduces background by a factor of ~2. We are left with a background rate which is a mix of other background events and events which were miscalculated, or misidentified, to be at the wrong position.

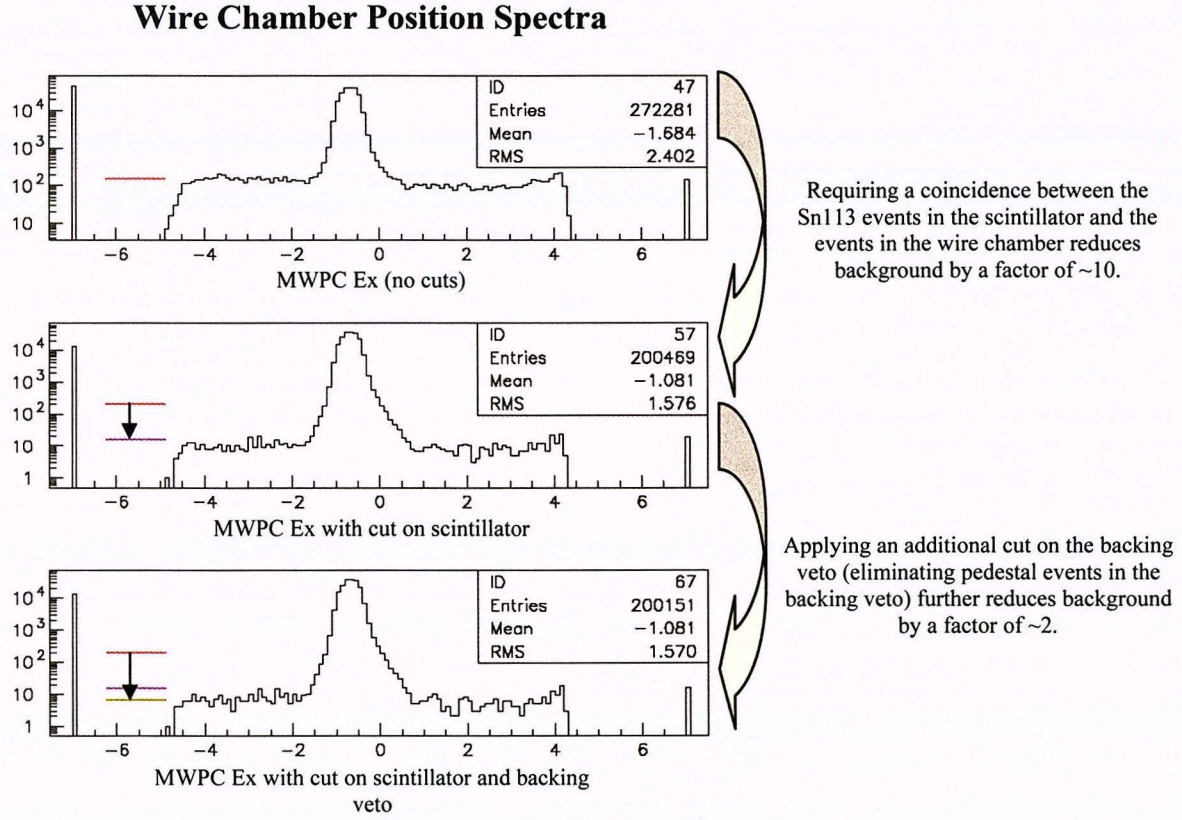

Figure 23 MWPC Position Spectra with various cuts on the background.

To determine the 95% confidence upper limit on the fraction of misidentified events, we calculate the difference between a theoretical estimate of the background due to the tail of the cosmic ray muon peak and the measured background in the MWPC position spectrum. This is done by using a background run (Run #2425) to determine what the ratio of the background in the scintillator spectrum in a range above our ^{113}Sn energy peak (essentially cosmic ray muons, range is from 5000:7500 channels) is, B1, to the background in the range where the ^{113}Sn energy peak would be if there were a tin source present (range is from 2500:7500 channels), B2. In a run with the source present (say Run #2309), we measure the # of events in the position peak, Npeak, from the position spectrum with a cut on the scintillator in the range 2500:5000 channels. In that same spectrum, we also measure all the events around that peak, Mmis. For the same source-present run, in a position spectrum with a cut on the scintillator in the higher range 5000:7500 channels, we measure the # of events in the same range as where we measured Mmis; we call

this Mcosm. All errors are Poisson statistics errors: (sqrt(N)). The theoretical estimate of the background due to the tail of the cosmic ray muon peak is then calculated by

$$\text{TheoreticalMmis} = (\text{Mcosm}*B1/B2) \pm \text{error1}.$$

The # of misidentified events is then

$$(\text{Mmis- Theoretical Mmis}) \pm \text{error2}$$

,where both error1 and error2 are determined by error propagation. The 95% confidence upper limit on the fraction of misidentified events is then

$$95\%\ \text{CL of misidentified events} = (\#\ \text{of Misidentified Events} + 2*\text{error2})/\text{Npeak}.$$

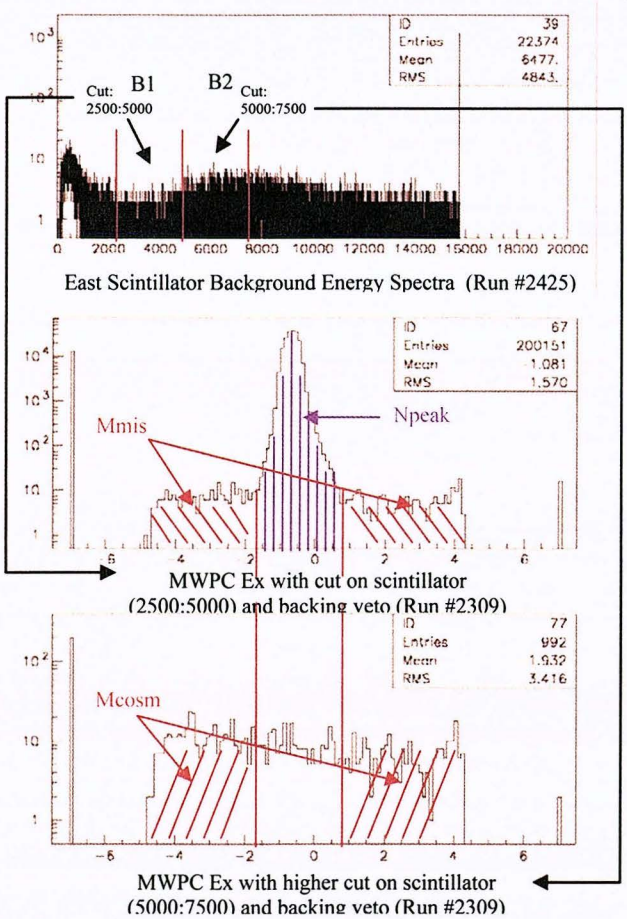

Theoretical Mmis = Mcosm *B1/B2 ± error1

Misidentified Events = (Mmis - Theoretical Mmis) ± error2

→ 95% CI of Misidentified Events =
(Misidentified Events +2*error2)/Npeak

Figure 24 Diagram depicting the calculation of a 95% CI of misidentified events. B1 is the # of events in the background spectra in the range 2500:5000, while B2 is the same but in the range 5000:7500. Npeak is the # of events in the position peak, Mmis is the # of events in the background of the position peak. Mcosm is the # of events in the same range as Mmis, but the spectrum has a higher cut (5000:7500) on the scintillator energy spectrum (this cut is the same as the B2 cut on the background spectrum). All errors are Poisson statistics errors: (sqrt(N)), and error1 and error2 are determined by the proper error propagation.

Run/Value	2309	2486	2313	2370
Ex 95% CI	0.000863	0.002288	0.006937	0.00088
Wx 95% CI	0.000682	0.002766	0.002027	0.004062
Ey 95% CI	0.003697	0.00947	0.003584	0.002834
Wy 95% CI	0.000946	0.003772	0.001758	0.005588
xn	0	-0.7	-2.3	1.7
yn	0	4.5	0	0
R	0	4.554119	2.3	1.7

Table 6 95% confidence upper limits on the fraction of misidentified events for various runs with different source positions.

Scintillator Energy Analysis

Another important calibration is the energy calibration of the scintillator. Both ^{113}Sn and ^{207}Bi have many conversion electron energy lines. However, there are only a few lines with high enough intensities which we can detect above background; these are listed in table 6. Each triplet (K, L, and M) of conversion electron lines creates one distinguishable peak in the data. ^{113}Sn has one peak, while ^{207}Bi has two.

These peaks were fit to Gaussians to determine their mean channel and corresponding uncertainty. The uncertainty was determined by considering both statistical deviations and systematic errors. The statistical errors we estimated as sigma/sqrt(N), where sigma is taken from the Gaussian fit, and N is the number of events in the energy peak; these errors were on the order of <1-5 channels. Fluctuations in the fit of the mean as we changed the range for the fit, on the order of 3 channels, were one source of systematic error. The greatest source of systematic error however came from the gain matching corrections. The spread in the scintillator PMT sum values, which we fitted to find the gain matching correction, is 214 channels for the east scintillator, and 301 for the west scintillator. Together, the errors on the east side provided a fairly good fit ($\chi^2 = 1.3$). However, they were too large of a spread on the west side ($\chi^2 = 0.15$).

The theoretical peak energy values are determined by calculating a mean weighted by intensity. Table 7 shows the conversion electron lines for ^{113}Sn and ^{207}Bi. Each triplet (K, L, M) of conversion electron lines creates a peak in the data. The peak energy for ^{113}Sn is 368.3 keV. The first peak energy for ^{207}Bi is 502.6, and the second peak energy is 994.6 keV. Figure 25 is an example of the energy spectra peaks.

$^{113}_{50}$Sn	Energy (keV)	Intensity (%)
1st peak: (K, L, M)		
CE K	363.758	28.4 %
CE L	387.461	5.57 %
CE M	390.872	1.108 %
$^{207}_{50}$Bi		
1st peak: (K, L, M)		
CE K	481.6935	1.515 %
CE L	553.8372	0.438 %
CE M	565.8473	0.147 %
2nd peak: (K, L, M)		
CE K	975.651	7.03 %
CE L	1047.795	1.84 %
CE M	1059.805	0.54 %

Table 7 Conversion Electron Lines for ^{113}Sn and ^{207}Bi. Each triplet (K, L, M) of conversion electron lines creates a peak in the data. ^{113}Sn has one visible peak above background, while ^{207}Bi has two. (Sonzogni)

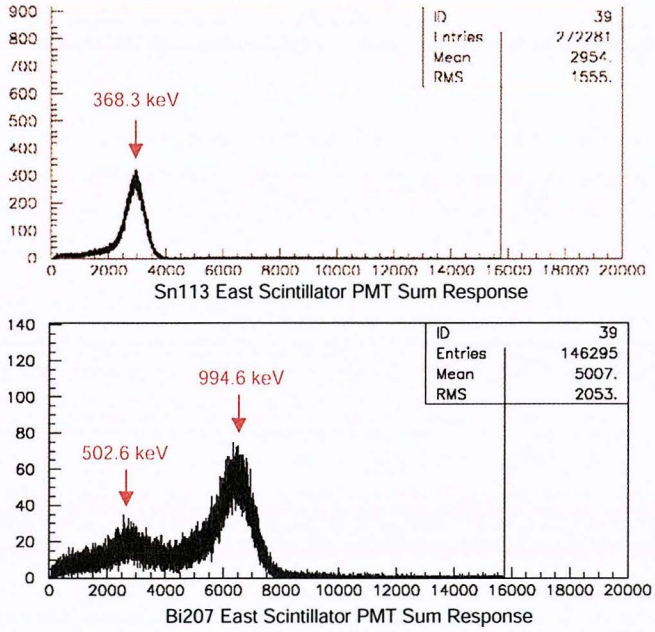

Figure 25 Scintillator PMT energy spectra for ^{113}Sn and ^{207}Bi.

Results

Here are the run-averaged position results for both the scintillator and the wire chamber. Both sets of scintillator histograms are comparisons between the zeroth order approximation and the theoretical correction applied to that approximation. In the first set, shown in figure 26, the runs are selected only for decent event rates (rates between 100 and 200 events/sec). Thus, we still have runs where the source is near the edge of the fiducial area and the correction for those runs far from the center actually places the reconstructed positions farther away from the nominal

position values. That is why we see that either the spread in the histograms for the corrected data, σ1, is not much smaller, or sometimes even larger than that of the zeroth order calculation, σ0. In the second set of scintillator histograms, shown in figure 27, the runs are additionally filtered so that we are left with runs where the source is within a 3cm radius of the center. Thus, almost all of these calculated positions improve when we apply the correction, and σ1 is generally smaller than σ0. Only the spread in the x position of the west detector increases slightly with the correction. This seems to be because the sigma is dominated mainly by the statistical spread in position, and not so much by the shape of the difference between the zeroth order approximation and the theoretical calculation of the position.

In the wire chamber, shown in figure 28, all the sigmas are reasonable (~0.35 cm), except for the y position difference histogram in the west detector. As of yet, we do not understand why the west y position spectra is so peculiar. This is an item for continuing research.

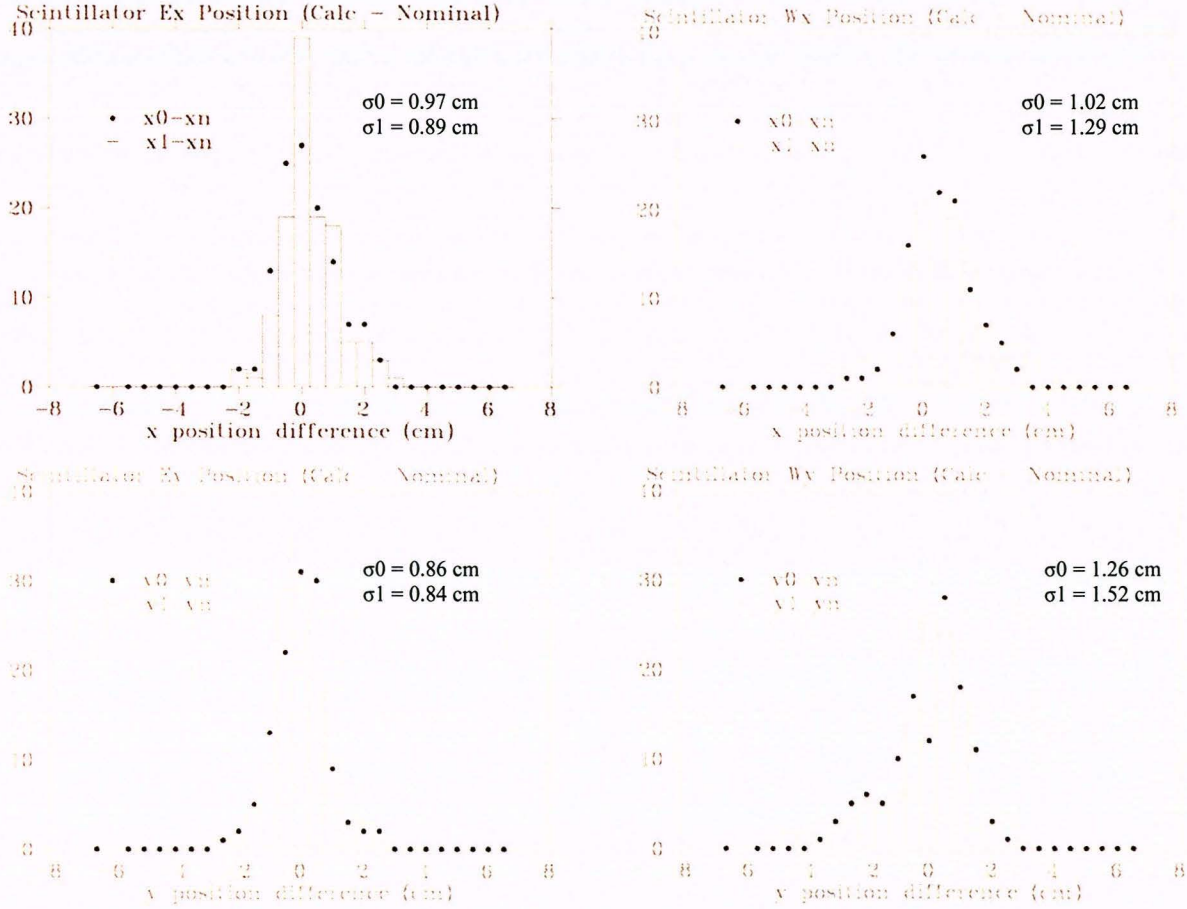

Figure 26 Scintillator Run-averaged position differences (calculated position – nominal position), for east and west, x and y. These runs are only selected for event rate between 100 and 200 events/sec. This does not guarantee that the correction x1 will be closer to the nominal value than the zeroth order calculation since our data shows that for runs near the edge of the fiducial region, the correction actually corrects in the wrong direction, making the resolution worse. We see that σ, or the resolution, in general increases with the correction.

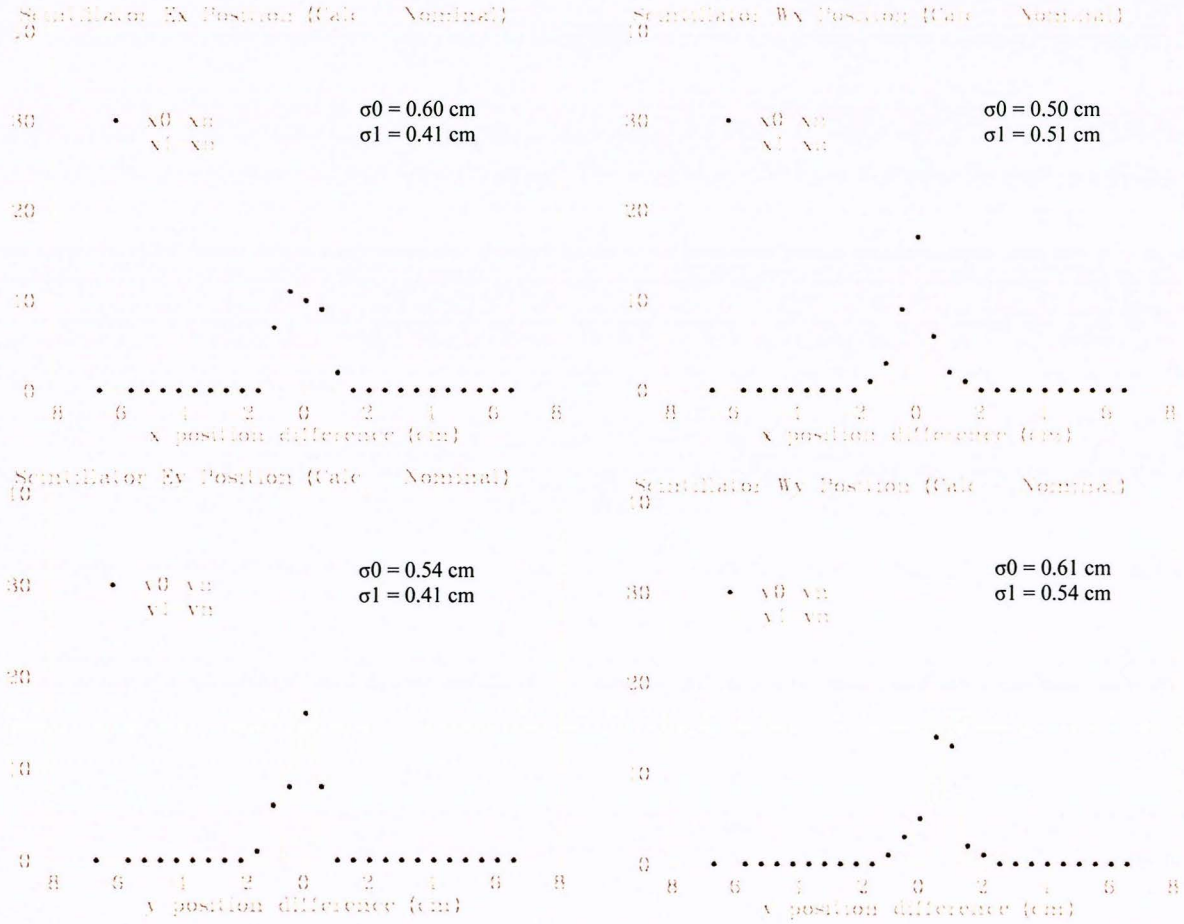

Figure 27 Scintillator Run-averaged position differences (calculated position – nominal position), for east and west, x and y. These runs are selected for event rate between 100 and 200 events/sec, and additionally for a nominal radius of <3cm. This guarantees that the correction x1 will be closer to the nominal value than the zeroth order calculation. Note that the resolution in general decreases with the correction.

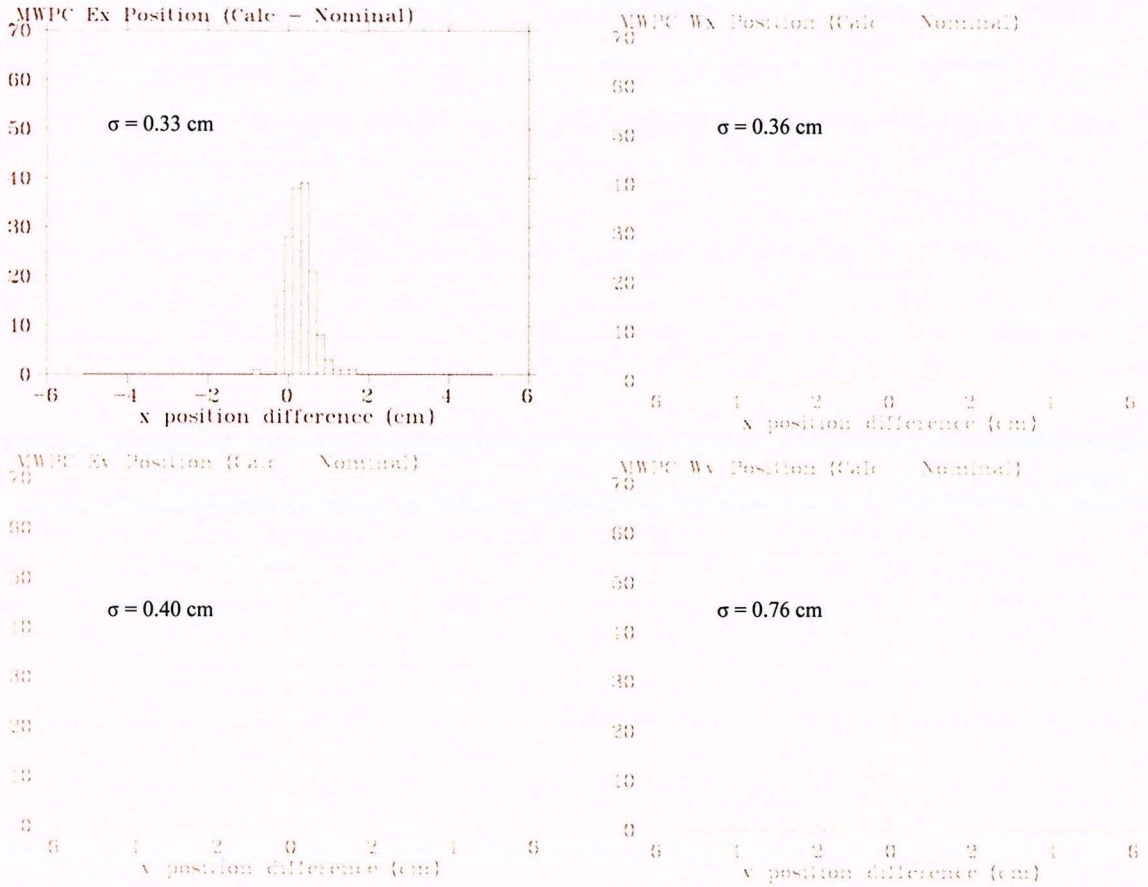

Figure 28 MWPC Run-averaged position differences (calculated position – nominal position), for east and west, x and y. All ^{113}Sn source runs are included. The spread of each histogram, a measure of the resolution, is given as σ.

Figures 29 and 30 show the event-by-event analysis position spectra for both the scintillator and the MWPC. All these values seem reasonable.

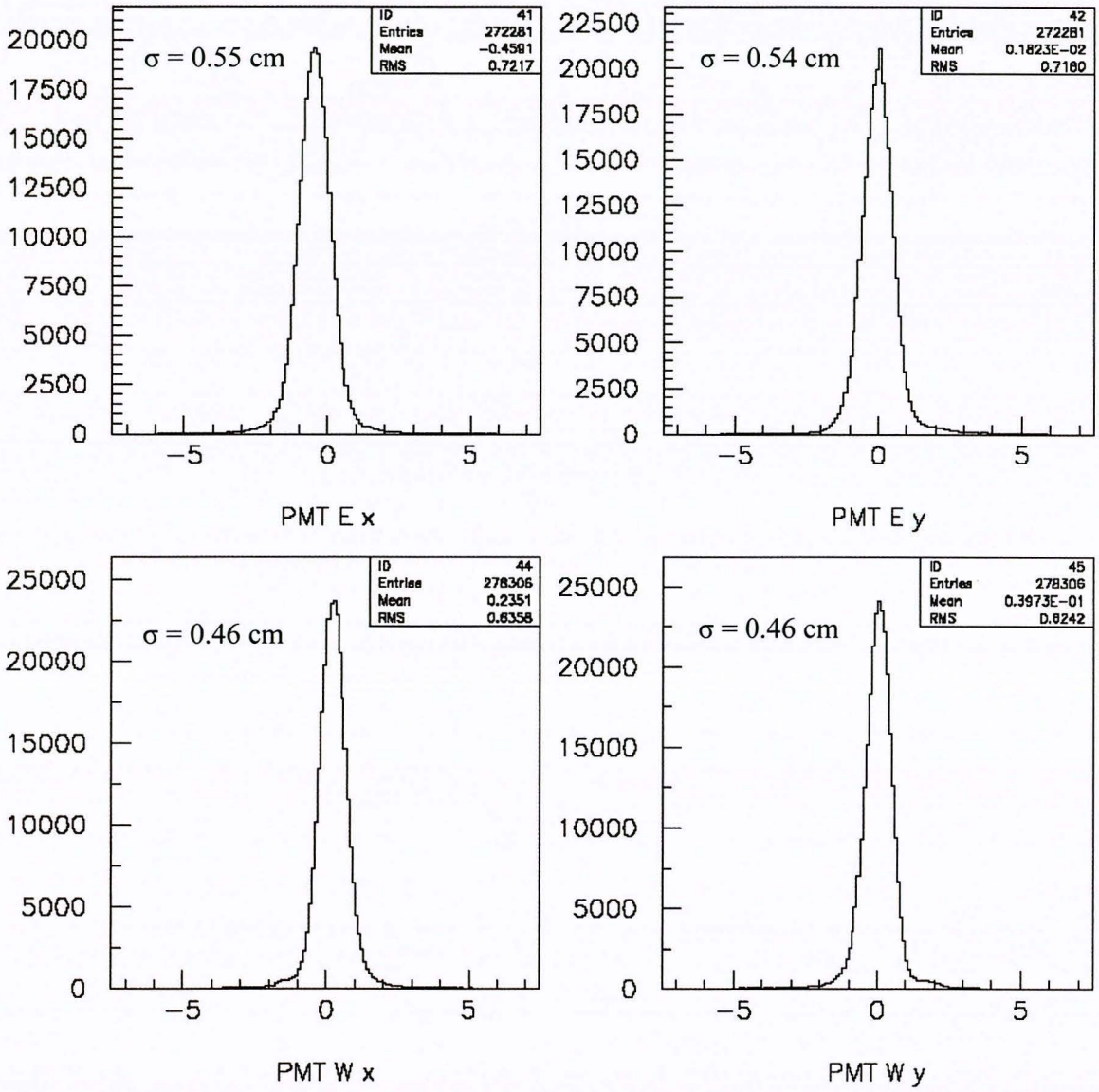

Figure 29 Scintillator positions in event-by-event analysis using zeroth order approximation calculation.

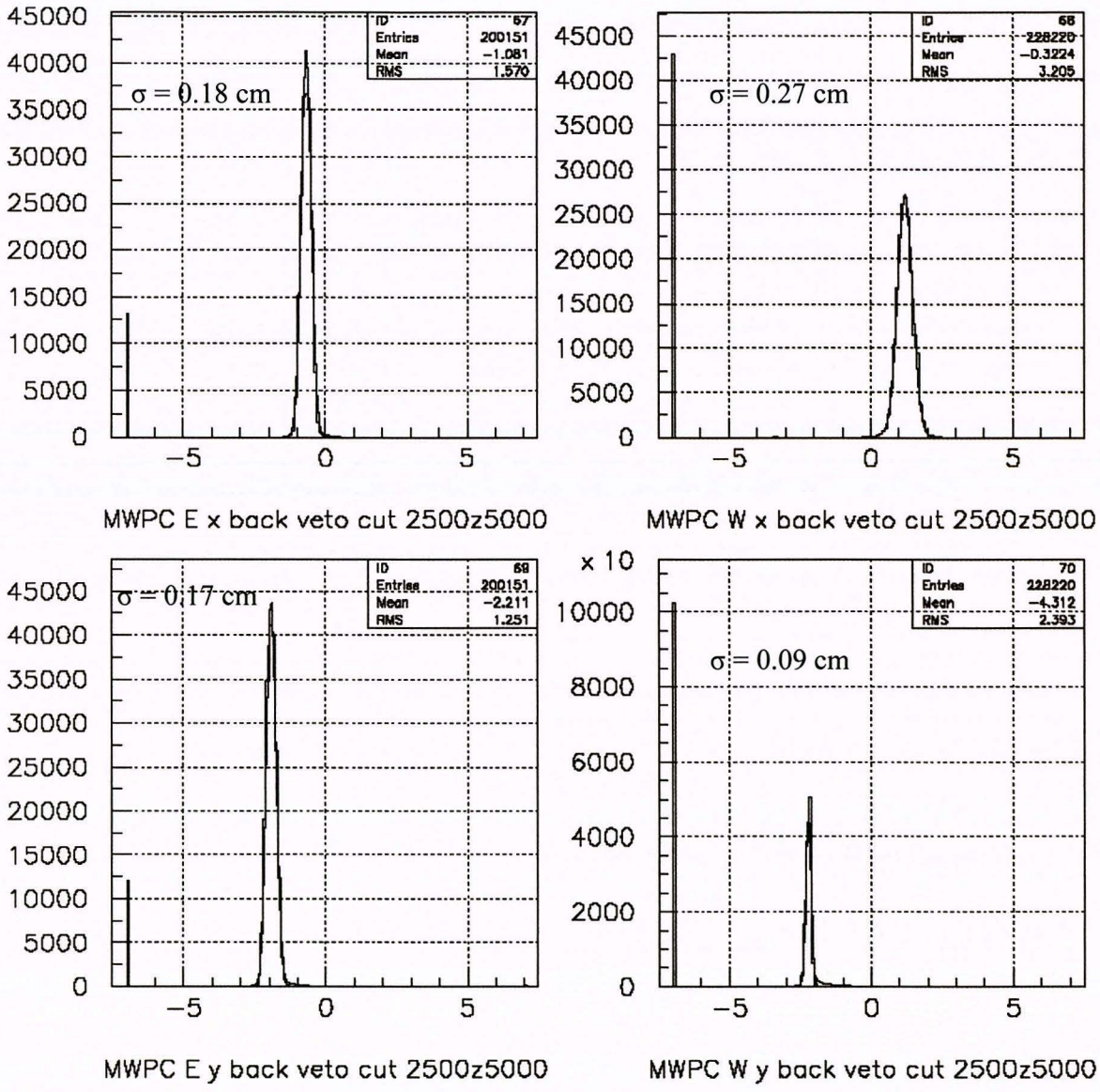

Figure 30 MWPC positions in event-by-event analysis.

Below is the energy response calibration of the scintillator. The fit seems fairly good for the east detector. However, the errors on the west side are too large, and so we have a small value for χ^2.

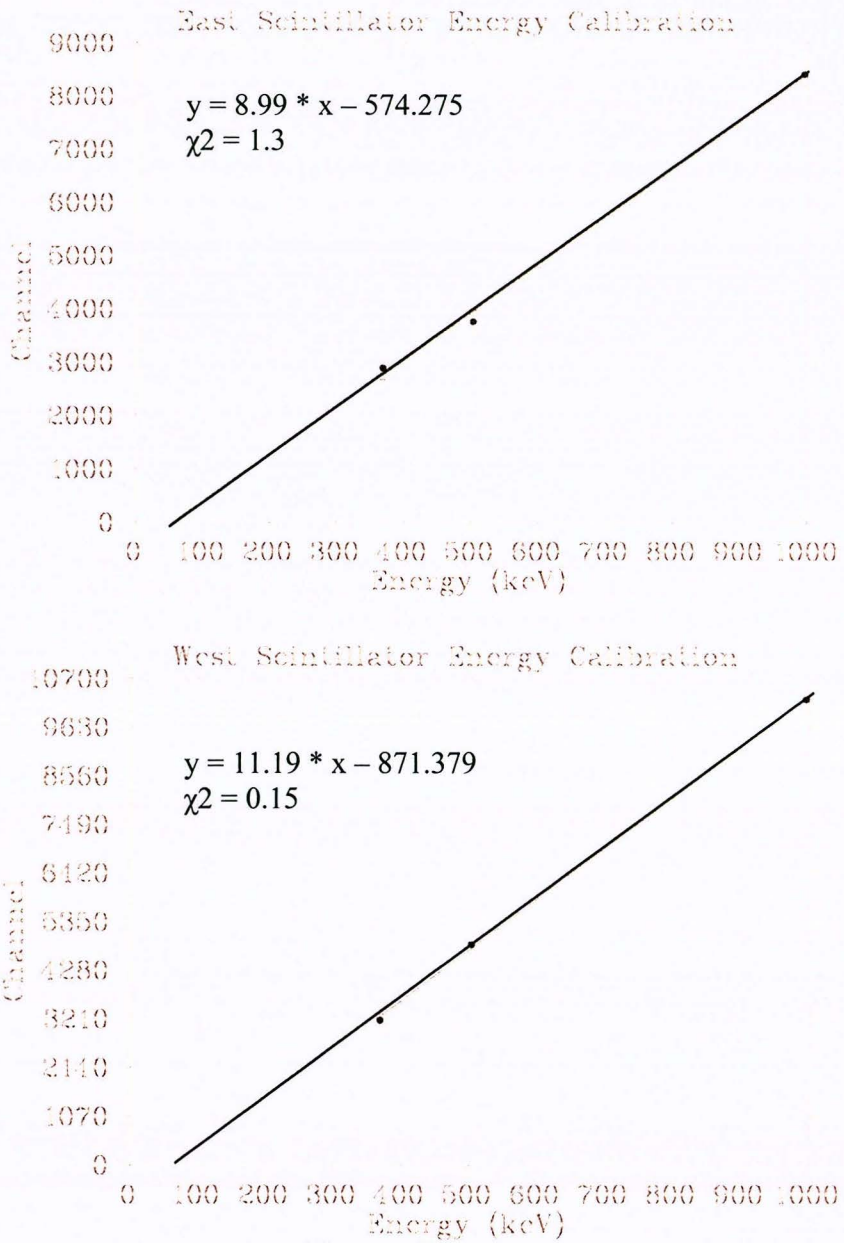

Figure 31 Energy Calibration fits for the ^{113}Sn and ^{207}Bi conversion electron lines. The errors on the west side are too large, and so we have a small value for χ^2.

Conclusions

UCNA is a precision measurement capable of testing the Standard Model. With these position and energy calibrations of the scintillator and wire chamber, we are ready to begin a measurement of A. The position resolution values for the wire chamber are what we were expecting from that detector. The main piece of new information is the position resolution we are able to get from the scintillator. By requiring timing and positional coincidence between the scintillator and wire chamber, this dual detector system should prove to be a powerful tool for determining the true position of neutron betas. For both detectors, it seems as though more detailed analysis and corrections for systematic errors can significantly improve the position resolution.

Specifically, comparisons to Monte Carlo simulations of the position resolution could help us understand additional physical affects of the system. In the west detector, we need to understand what is causing some peculiar shaping of the peak in the wire chamber position spectra (perhaps we need to come up with better ways to fix the "bad" cathode wires). A more detailed investigation of the possible rotation of the 1 Tesla magnetic field in the x plane will also need to be conducted.

Sources

Purcell, Edwards. *Electricity and Magnetism.* Boston, Massachusetts: McGraw-Hill, Inc., 1985.

Sonzogni, Alejandro. "Chart of Nucleotides." National Nuclear Data Center. Apr. 18 2006. <http://www.nndc.bnl.gov/chart/>.

UCNA Collaboration. "Technical Review Report for an Accurate Measurement of the Neutron Spin – Electron Angular Correlation in Polarized Neutron Beta Decay with Ultra-Cold Neutrons." Apr. 11, 2000. <http://www.krl.caltech.edu/ucn/physics.html>.

Acknowledgements

I would like to thank my mentor, Professor Bradley W. Filippone, for the opportunity to pursue this research, and for his great enthusiasm and patience in monitoring the project's progress. I would also like to thank my co-mentor, Brad Plaster, who guided me through the challenges of research at Los Alamos; Junhua Yuan for his expertise and help with PAW and ROOT; and the UCNA Collaboration for supporting me and allowing me to participate in this experiment.

Appendix

Summary of ntuple variables for β-detector analysis

B. Plaster

Last revised: April 5, 2006

Event-wise variables

Variable	Description
sis00	Input register [= 1 (= 2) for two-fold east (west) β-PMT trigger]
s8300	Clock (scaler) stamped in μs [reset by proton pulse, if applicable]

β-scintillator variables

Variable	Description
QADC0	QADC channel number for east β-scintillator PMT #1
QADC1	QADC channel number for east β-scintillator PMT #2
QADC2	QADC channel number for east β-scintillator PMT #3
QADC3	QADC channel number for east β-scintillator PMT #4
QADC4	QADC channel number for west β-scintillator PMT #1
QADC5	QADC channel number for west β-scintillator PMT #2
QADC6	QADC channel number for west β-scintillator PMT #3
QADC7	QADC channel number for west β-scintillator PMT #4
TDC00	TDC channel number for east β-scintillator PMT #1
TDC01	TDC channel number for east β-scintillator PMT #2
TDC02	TDC channel number for east β-scintillator PMT #3
TDC03	TDC channel number for east β-scintillator PMT #4
TDC08	TDC channel number for west β-scintillator PMT #1
TDC09	TDC channel number for west β-scintillator PMT #1
TDC10	TDC channel number for west β-scintillator PMT #1
TDC11	TDC channel number for west β-scintillator PMT #1
tdc016	TDC channel number for east two-fold β-PMT trigger
tdc017	TDC channel number for west two-fold β-PMT trigger

μ-veto variables

Variable	Description
QADC8	QADC channel number for east backing veto
TDC018	TDC channel number for east backing veto
QADC9	QADC channel number for east top veto
TDC019	TDC channel number for east top veto
QADC10	QADC channel number for west backing veto
TDC020	TDC channel number for west backing veto

East MWPC variables

Variable	Description	Ganged position [mm]
pdc20	Anode PADC channel number	—
pdc22	Cathode PADC channel number	$y = +66.04$
pdc23	Cathode PADC channel number	$y = +55.88$
pdc24	Cathode PADC channel number	$y = +45.72$
pdc25	Cathode PADC channel number	$y = +35.56$
pdc26	Cathode PADC channel number	$y = +25.40$
pdc27	Cathode PADC channel number	$y = +15.24$
pdc28	Cathode PADC channel number	$y = +5.08$
pdc29	Cathode PADC channel number	$y = -5.08$
pdc210	Cathode PADC channel number	$y = -15.24$
pdc211	Cathode PADC channel number	$y = -25.40$
pdc212	Cathode PADC channel number	$y = -35.56$
pdc213	Cathode PADC channel number	$y = -45.72$
pdc214	Cathode PADC channel number	$y = -55.88$
pdc215	Cathode PADC channel number	$y = -66.04$
pdc218	Cathode PADC channel number	$x = +66.04$
pdc219	Cathode PADC channel number	$x = +55.88$
pdc220	Cathode PADC channel number	$x = +45.72$
pdc221	Cathode PADC channel number	$x = +35.56$
pdc222	Cathode PADC channel number	$x = +25.40$
pdc223	Cathode PADC channel number	$x = +15.24$
pdc224	Cathode PADC channel number	$x = +5.08$
pdc225	Cathode PADC channel number	$x = -5.08$
pdc226	Cathode PADC channel number	$x = -15.24$
pdc227	Cathode PADC channel number	$x = -25.44$
pdc228	Cathode PADC channel number	$x = -35.56$
pdc229	Cathode PADC channel number	$x = -45.72$
pdc230	Cathode PADC channel number	$x = -55.88$
pdc231	Cathode PADC channel number	$x = -66.04$

West MWPC variables

Variable	Description	Ganged position [mm]
padc0	Anode PADC channel number	—
padc2	Cathode PADC channel number	$y = +66.04$
padc3	Cathode PADC channel number	$y = +55.88$
padc4	Cathode PADC channel number	$y = +45.72$
padc5	Cathode PADC channel number	$y = +35.56$
padc6	Cathode PADC channel number	$y = +25.40$
padc7	Cathode PADC channel number	$y = +15.24$
padc8	Cathode PADC channel number	$y = +5.08$
padc9	Cathode PADC channel number	$y = -5.08$
padc10	Cathode PADC channel number	$y = -15.24$
padc11	Cathode PADC channel number	$y = -25.40$
padc12	Cathode PADC channel number	$y = -35.56$
padc13	Cathode PADC channel number	$y = -45.72$
padc14	Cathode PADC channel number	$y = -55.88$
padc15	Cathode PADC channel number	$y = -66.04$
padc18	Cathode PADC channel number	$x = -66.04$
padc19	Cathode PADC channel number	$x = -55.88$
padc20	Cathode PADC channel number	$x = -45.72$
padc21	Cathode PADC channel number	$x = -35.56$
padc22	Cathode PADC channel number	$x = -25.40$
padc23	Cathode PADC channel number	$x = -15.24$
padc24	Cathode PADC channel number	$x = -5.08$
padc25	Cathode PADC channel number	$x = +5.08$
padc26	Cathode PADC channel number	$x = +15.24$
padc27	Cathode PADC channel number	$x = +25.44$
padc28	Cathode PADC channel number	$x = +35.56$
padc29	Cathode PADC channel number	$x = +45.72$
padc30	Cathode PADC channel number	$x = +55.88$
padc31	Cathode PADC channel number	$x = +66.04$